Pathological mutations reveal the key role of the iRhom2 N-terminus for ADAM17 binding, stability and activity.

Katharina Bläsius[1*], Lena Ludwig[1*], Sarah Knapp[2], Charlotte Flaßhove[1], Friederike Sonnabend[1], Diandra Keller[1], Nikola Tacken[1], Xintong Gao[1], Selcan Kahveci-Türköz[1], Caroline Grannemann[1], Aaron Babendreyer[1], Colin Adrain[3], Sebastian Huth[4], Jens Malte Baron[4], Andreas Ludwig[1], Stefan Düsterhöft[1#]

[1] Institute of Molecular Pharmacology, Medical Faculty, RWTH Aachen University, Aachen, Germany

[2] Institute of Biochemistry and Molecular Biology, Medical Faculty, RWTH Aachen University, Aachen, Germany

[3] Patrick G Johnston Centre for Cancer Research, Queen's University, Belfast, N. Ireland

[4] Department of Dermatology and Allergology, Medical Faculty, RWTH Aachen University, Aachen, Germany

corresponding author

* authors contributed equally

Abstract

The protease ADAM17 plays an important role in inflammation and cancer and is regulated by iRhom2. Mutations in the cytosolic N-terminus of human iRhom2 cause tylosis with oesophageal cancer (TOC). In mice, partial deletion of the N-terminus results in a curly hair phenotype (cub). These pathological consequences are consistent with our findings that iRhom2 is highly expressed in keratinocytes and in oesophageal cancer. Cub and TOC are associated with hyperactivation of ADAM17-dependent EGFR signalling. However, the underlying molecular mechanisms are not understood. We have identified a regulatory site, encompassing all known TOC mutations, whose disruption increases constitutive ADAM17 activity. The larger cub deletion also includes the TOC site and thus also promotes increased constitutive ADAM17 activity. Furthermore, the cub mutation, but not the TOC mutation, causes severe reductions in stimulated shedding, binding and stability of ADAM17, suggesting the presence of additional regulatory sites in the N-terminus of iRhom2. Overall, this study contrasts the TOC and cub mutations, illustrates their different molecular consequences and reveals important key functions of the iRhom2 N-terminus in regulating ADAM17.

Key words: esophageal squamous cancer, ectodomain shedding, EGFR ligand release, curly-bare (cub) mouse, iRhom2, ADAM17, Howel–Evans syndrome, tylosis with oesophageal cancer (TOC)

Introduction

Oesophageal cancer (OC) is a critical global health concern, given its alarming prognosis and high mortality rate, ranking as the sixth leading cause of cancer-related death worldwide. Oesophageal squamous cell carcinoma (OSCC) and oesophageal adenocarcinoma (OAC) are the primary histological subtypes of OC. Despite their similarities, OSCC and OAC differ both epidemiologically and biologically (Rizza et al., 2015, Smyth et al., 2017, Uhlenhopp et al., 2020). The prognosis for OSCC, which comprises most OC cases, is exceptionally poor (Uhlenhopp et al., 2020, Yang et al., 2022). Notably, smoking and alcohol consumption serve as significant risk factors for OSCC development. However, the underlying molecular and genetic mechanisms driving OC remain poorly understood.

Howel-Evans syndrome, also called tylosis with oesophageal carcinoma (TOC), directly correlates with an increased risk to develop OSCC (Howel-Evans et al., 1958, Blaydon et al., 2012). This rare genetic disorder affects the seven-transmembrane spanning pseudoprotease iRhom2 (Fig. 1A) and its functions, altering EGF receptor (EGFR) signalling pathways by aggravating iRhom2-dependent ectodomain shedding (Blaydon et al., 2012).

Shedding, the proteolytic release of ectodomains from membrane proteins, is a crucial mechanism in many physiological and pathological processes. The released soluble ectodomains, which are often receptors or receptor ligands, exhibit potent biological activity. iRhoms, pseudoproteases of the rhomboid family, play a crucial role in the shedding process by forming a complex with the transmembrane sheddase ADAM17 (A-disintegrin and metalloproteinase 17)(Siggs et al., 2012, Christova et al., 2013, Siggs et al., 2014, Li et al., 2015).

ADAM17 has a broad spectrum of substrates, including cytokines, growth factors and cytokine receptors such as tumour necrosis factor (TNF)(Black et al., 1997), transforming growth factor α (TGFα) and amphiregulin (AREG)(Peschon et al., 1998, Sahin et al., 2004). Release of these substrates is crucially involved in various (patho-)physiological processes (Peschon et al., 1998, Blaydon et al., 2011) highlighting the central role of ADAM17 in development and in the immune response but also in chronic inflammation and cancer. Additionally, the multi-faceted role of ADAM17 in virus entry has been recently demonstrated (Lambert et al., 2005, Palau et al., 2020, Yuan et al., 2021, Jocher et al., 2022, Niehues et al., 2022, Zaruba et al., 2022).

The formation of the iRhom-ADAM17 complex is a necessary step for ADAM17 maturation (Fig. 1A,B)(Christova et al., 2013, Maretzky et al., 2013, Grieve et al., 2017, Düsterhöft et al., 2021, Kahveci-Türköz et al., 2023). On the cell surface the shedding activity of mature ADAM17 is further regulated by iRhoms (Cavadas et al., 2017, Grieve et al., 2017). In mammals, two genes for iRhoms exist: RHBDF1 (iRhom1) and RHBDF2 (iRhom2). While iRhom1 is present in most cell types, iRhom2 initially appeared to be immune cell specific, but is also upregulated during inflammatory episodes in

70 other cell lineages such as endothelial and epithelial cells (Lu et al., 2017, Babendreyer et al., 2020,
71 Giese et al., 2021). Consistent with this, iRhom2 deficiency in mice and humans does not cause obvious
72 developmental defects, but impairs the immune response (Adrain et al., 2012, McIlwain et al., 2012,
73 Kubo et al., 2022).

74 iRhoms contain a large N-terminal cytosolic tail that has not yet been fully characterised (Fig. 1A). The
75 genetic disorder causing TOC is caused by single point mutations in the N-terminus (Howel-Evans et
76 al., 1958, Ellis et al., 1994, Blaydon et al., 2012, Saarinen et al., 2012, Ellis et al., 2015, Mokoena et al.,
77 2018). This disorder is characterised by symptoms such as leukoplakia and hyperkeratosis and
78 increases the risk of OSCC (Chao-Chu et al., 2021). The mutations are classified as "gain of function"
79 because they apparently upregulate ADAM17 activity, resulting in higher levels of EGFR ligands, EGFR
80 hyperactivation in keratinocytes and increased release of TNF receptor 1, leading to reduced apoptosis
81 (Blaydon et al., 2012, Maney et al., 2015, Hosur et al., 2018b).

82 In mice, a spontaneous mutation called cub (curly-bare) results in a deletion of 268 amino acid residues
83 of the N-terminus including the TOC mutation positions, causing aberrant hair growth, hyperkeratosis
84 and hyperproliferative wound healing (Johnson et al., 2003, Siggs et al., 2014, Hosur et al., 2018a). This
85 cub deletion was linked to higher ADAM17-mediated shedding of AREG. However, different studies
86 contested the notion that the cub mutation results in higher ADAM17 activity at least in i*n vitro* settings
87 (Siggs et al., 2014, Hosur et al., 2018a). Interestingly, mice carrying TOC mutations exhibit the same
88 skin-related phenotype as cub mice (Hosur et al., 2017, Hosur et al., 2018a, Hosur et al., 2018b).
89 Noteworthy, the deficiency in iRhom2 in mice seems to cause a thinning of epidermis in the footpad
90 (Maruthappu et al., 2017). The phenotype of both, cub and TOC mice, can be rescued by AREG
91 deficiency, suggesting a similar underlying process with increased AREG-dependent signalling (Hosur
92 et al., 2018b). However, the molecular mechanism for these mutations remains unknown.

93 Only a few regulatory regions have been identified within the N-terminus of iRhom2, including
94 phosphorylation sites that facilitate binding of members of the 14-3-3 protein family (Cavadas et al.,
95 2017, Grieve et al., 2017). Deletion of the entire N-terminus appears to destabilise the iRhom-ADAM17
96 complex, resulting in loss of mature ADAM17. The adapter protein FRMD8, also known as iTAP (iRhom
97 tail-associated protein) has been identified as an essential binding partner of the N-terminus of iRhom,
98 which has a stabilising function for iRhom and thus for the iRhom-ADAM17 complex (Künzel et al.,
99 2018, Oikonomidi et al., 2018). This seems to explain the loss of mature ADAM17 when the N-terminus
100 is missing. Notably, part of this FRMD8-binding region is lost in the cub deletion, while the TOC
101 mutations lie outside this region. Recently, it was shown that the N-terminus is cleaved off by a signal
102 peptidase complex and migrates to the nucleus, where it influences gene expression (Dulloo et al.,
103 2022, Zanotti et al., 2022).

104 In this study, we observed high expression levels of iRhom2 in skin tissue samples and primary
105 keratinocytes under physiological conditions, providing an explanation for the distinct skin-related
106 phenotype in humans and mice with TOC or cub, respectively. Notably, iRhom2 and ADAM17
107 expression levels were significantly upregulated in OSCC patient samples, which is consistent with the
108 higher risk for OSCC in TOC patients.

109 It is important to separate the direct molecular effects of both mutation types (single point mutation
110 vs large deletion) on the functions of the iRhom2-ADAM17 complex from downstream effects: *In vivo*,
111 altered ADAM17 activity and the mutated soluble iRhom2 N-terminus in the nucleus will have long-
112 term effects on gene expression as well as ADAM17-dependent signalling pathways. Here, we focused
113 on the direct molecular consequences of the TOC single point mutations and the large cub deletion.
114 We identified a highly conserved motif that contains all known TOC sites and exhibits features of a
115 regulatory interaction site. Disruption of this site results in loss of regulation of ADAM17 activity,
116 leading to increased constitutive shedding. The cub deletion covers a larger part of the N-terminus,
117 including the TOC site. Therefore, the cub deletion also causes higher constitutive shedding activity of
118 ADAM17. However, the cub deletion loses the ability to promote stimulated/activatable ADAM17
119 activity. In addition, we found that this deletion decreases binding to ADAM17 and causes accelerated
120 degradation of ADAM17.

121 Overall, our results provide deeper insights into the molecular mechanisms controlling the iRhom2-
122 ADAM17 complex through the N-terminus of iRhom2 by demonstrating a distinct effect of TOC site
123 disruption, in contrast to the multiple overlapping and therefore more severe effects of the cub
124 deletion.

125

126

127 **Results**

128

129 **iRhom2 expression levels are high in skin and OSCC**

130 The observed phenotypes of iRhom2 deficiency and cub deletion, as well as the pathologies associated
131 with the human TOC mutations, clearly point to a central role of iRhom2 in epidermal tissue. While
132 high iRhom2 expression is often primarily associated with immune cells, its expression pattern in the
133 epidermis is not yet well defined. Hence, we analysed gene expression data from skin biopsies of
134 healthy individuals obtained from publicly available microarray data (Hruz et al., 2008). We indeed
135 observed a robust expression of iRhom2 in the skin samples (Fig. 1C). Moreover, primary human
136 keratinocytes have significantly higher levels of iRhom2 expression compared to primary fibroblasts,

artery smooth muscle cells, and bronchial smooth muscle cells (Fig. 1C). Notably, the ratio of iRhom2 to iRhom1 is substantially higher in keratinocytes than in other primary cell types (Fig. 1C; Fig. S1A), indicating a pivotal role for iRhom2 in regulating ADAM17 activity in keratinocytes *in vivo*. To verify the microarray data, we analysed iRhom1 and iRhom2 protein levels via immunoblotting and gene expression via RT-qPCR in primary keratinocytes and fibroblasts. Indeed, in agreement with the microarray data, we found higher protein levels and gene expression of iRhom2 in keratinocytes compared to fibroblasts (Fig. 1D,E). This expression pattern aligns with the predominantly skin-related manifestations of TOC and cub. We found a similar pattern in murine primary keratinocytes, again highlighting iRhom2's importance in regulating ADAM17 activity in the skin (Fig. S1B).

Considering the known induction of iRhom2 expression in response to proinflammatory stimuli (Babendreyer et al., 2020, Giese et al., 2021), we investigated whether the observed iRhom2 expression patterns in primary keratinocytes were due to pre-activation by proinflammatory conditions. We found a significant increase in iRhom2 gene expression in primary keratinocytes 24 hours after treatment with proinflammatory stimuli, while iRhom1 showed no such elevation (Fig. 1F). This finding supports that the high iRhom2 expression in primary keratinocytes is likely the basal level under physiological conditions which can be further increased under inflammatory conditions. Furthermore, the gene expression pattern of untreated keratinocytes is also consistent with the basal iRhom2 and iRhom1 gene expression pattern in healthy human skin biopsies (Fig. 1C).

Since TOC mutations also pose an increased risk of developing OSCC, we examined iRhom2 expression in OSCC samples and compared them to healthy oesophagus squamous tissue, as well as samples from OAC and a premalignant condition, called Barrett's oesophagus. In OSCC samples, we observed a significant upregulation of iRhom2, accompanied by a downregulation of iRhom1, compared to healthy oesophagus squamous tissue (Fig. 1G). The ratio of iRhom2 to iRhom1 was four times higher in OSCC samples than in the healthy tissue. While OAC samples also showed a significantly elevated iRhom2-iRhom1 ratio, the increase was less pronounced (Fig. 1G). On the other hand, samples from Barrett's oesophagus exhibited no change in the ratio but displayed an overall reduction in iRhom1 and iRhom2 gene expression. Furthermore, we found a significant upregulation of ADAM17 gene expression exclusively in OSCC samples (Fig. S1C). In contrast, ADAM10, a close relative of ADAM17 with partially overlapping substrate spectrum and independent of iRhom functions, did not show this expression pattern (Fig. S1C). The gene expression of EGFR ligands, TGFα and AREG, crucial ADAM17 substrates, did not show significant changes in OSCC compared to healthy tissue (Fig. S1C). To ensure that the elevated levels of iRhom2 in OSCC were not due to persistent proinflammatory conditions or the presence of tumour microenvironment-associated immune cells, we examined proinflammatory markers and immune cell markers. We observed no significantly elevated gene expression of TNF or IL6 (Fig. S1C), and only minimal gene expression of CD14, suggesting the presence of some

172 monocytes/macrophages in the samples but not in sufficient quantities to explain the high iRhom2
173 levels in OSCC (Fig. S1D; Fig. S2A,B).

174 In summary, the gene expression patterns of iRhom2 and ADAM17 support the notion of an important
175 role for iRhom2-dependent ADAM17 activity in both skin and OSCC, which is consistent with the
176 pathological consequences of TOC single point mutations and cub deletion.

177

178 The N-terminal tail represents a large intrinsically disordered part of iRhom2.

179 To investigate the molecular mechanisms underlying the functions of the N-terminal tail of iRhom2, we
180 performed *in silico* structural studies. Our bioinformatic analyses predict that the N-terminal tail of
181 iRhom2 has a largely unstructured/intrinsically disordered nature (Fig. 2A), which is typical for protein-
182 protein interaction interfaces (Dyson, 2016, Arakawa et al., 2023). Using the A.I.-based AlphaFold2
183 algorithm, we predicted the structural makeup of the N-terminus, which revealed an overall low pLDDT
184 and PAE, again confirming a lack of higher structural regions (Fig. 2B-D). Some isolated secondary
185 structures were predicted, but the N-terminus seems to be primarily intrinsically disordered (Fig. 2A-
186 F), which is a hallmark to promote protein-protein interaction.

187 However, while the N-terminus seems to play a crucial role in regulating the iRhom-ADAM17 complex,
188 only a handful of direct interactors such as FRMD8, ERK2, and 14-3-3 proteins have been identified
189 (Fig. 1A)(Cavadas et al., 2017, Grieve et al., 2017, Künzel et al., 2018, Oikonomidi et al., 2018,
190 Schumacher et al., 2023). Using ANCHOR2, we have identified an additional region that is highly likely
191 to be an interface for protein-protein interactions (Fig. 2E). Strikingly, this region is highly conserved
192 and includes all known TOC mutation positions (Fig. 2E-F). In addition, R192 in the middle of this TOC
193 site was found to be methylated in human iRhom2 by three independent high-throughput proteomic
194 screens (Figure 2F)(Guo et al., 2014, Hornbeck et al., 2015). This further supports the TOC site as a
195 regulatory interaction site, as protein methylation is a hallmark of protein interaction sites.

196 Furthermore, our bioinformatic analysis of the N-terminus of iRhom2 also indicates the presence of a
197 nuclear localisation sequence (NLS), which is consistent with recent observations of its translocation to
198 the nucleus after cleavage by the signal peptidase complex (Fig. 2G)(Dulloo et al., 2022).

199 Overall, the N-terminal tail represents a large intrinsically disordered region that provides distinct hubs
200 for regulation and interaction. Furthermore, all known TOC mutations are part of a predicted protein-
201 protein interaction site.

202

The TOC mutations and the cub deletion result in distinct molecular consequences for mature ADAM17.

To gain a comprehensive understanding of the regulatory system acting on the iRhom2-ADAM17 complex, it is important to understand the molecular similarities and differences between the TOC single point mutations and cub deletions, as they exhibit a strikingly similar phenotype in mice (Hosur et al., 2018b). While the TOC mutations affect a distinct region, the cub deletion affects a large part of the N-terminal tail encompassing different known regulatory and interaction sites such as two phosphorylation sites, the TOC region as well as the ERK2 binding site (Fig. 2G). The exact binding site of the FRMD8 interaction is not yet known, but the approximate binding region was mapped before (Fig. 2G)(Künzel et al., 2018, Oikonomidi et al., 2018). Hence, in contrast to TOC mutations the cub deletion affects most likely more regulatory aspects. To further dissect the molecular regulations of iRhom2 and its dysregulation, we designed an additional N-terminal deletion (nd197) that still contains the FRMD8 binding region and therefore retains binding to endogenous FRMD8 (Fig. 2G,H). In contrast, we could not detect FRMD8 binding for the cub deletion. We created two additional deletions (nd349 and nd370) with almost the entire N-terminus removed (Fig. 2G,H) to compare the effect of complete loss of the N-terminal tail with the partial deletions. We also hypothesised that the TOC single point mutations only gradually affect the function of the identified TOC site (Fig. 2E). Hence, we designed the deletion ndTOC (Δ182-192) to remove most of the TOC site (Fig. 2E-F). As expected, binding to FRMD8 in iRhom2 is not altered by either the TOC point mutation (I186T) or the deletion of the TOC site (ndTOC) compared to wt-iRhom2 (Fig. 2I).

The TOC mutations are autosomal dominant and the cub deletion leads to a phenotype already in heterozygosity. To analyse the direct molecular effects of these iRhom2 variants on ADAM17 regulation in combination with wt-iRhoms, we used HEK293 cells with endogenous iRhom1 and iRhom2 (Fig. S1E) as an already established and widely used model system (Cavadas et al., 2017, Sieber et al., 2022, Kahveci-Türköz et al., 2023), with epithelial morphology (Inada et al., 2016).

As iRhom levels are a rate limiting factor for forward transport and maturation of ADAM17, increased expression of either human or murine wt-iRhom2 results in more mature ADAM17 (Fig. 3A-C), as shown before (Düsterhöft et al., 2021, Kahveci-Türköz et al., 2023). Consequently, the amount of mature ADAM17 on the cell surface is also elevated (Fig. 3D,E). In contrast, expression of the murine iRhom2 cub deletion does not promote higher levels of mature ADAM17 (Fig. 3A). Furthermore, the three deletions nd197, nd349 and nd370 showed also a significant decrease in mature ADAM17 levels compared to wt-iRhom2 (Fig.3 B). We also observed a significant reduction in total ADAM17 levels in cells expressing these deletions compared to wt-iRhom2 or the negative control (Fig. 3A,B). In line with these findings the amount of mature ADAM17 on the surface was also lower in cells expressing the

237 deletions compared to both wt-iRhom2 and even control cells (Fig. 3D), although the deletion
238 constructs can be detected on the cell surface similarly to wt-iRhom2 (Fig. S3B). Notably, these effects
239 seem to be FRMD8 independent since nd197 still binds endogenous FRMD8 (Fig. 2H).

240 Expression of iRhom2 with a human TOC mutation (I186T) or a deletion of the TOC site (ndTOC) also
241 shows a reduced amount of mature ADAM17 compared to wt-iRhom2 (Fig. 3C). ndTOC seems to lead
242 to an even stronger reduction than the single point mutation, suggesting that the complete deletion of
243 the TOC site has a stronger effect than the single point mutation (Fig. 3C). However, in contrast to the
244 larger deletions (nd187, cub, nd349 and nd379), we did not observe a reduction in the total amount of
245 ADAM17 (Fig. 3C). Both iRhom2_I186T and ndTOC exhibit a cell surface presence similar to that of the
246 wt-iRhom2 (Fig. S3C). iRhom2_I186T leads to increased ADAM17 surface localisation compared to
247 control cells and the impact on surface ADAM17 levels is not significantly different to cells with wt-
248 iRhom2 expression (Fig. 3E). Remarkably, ndTOC expression results in significantly lower levels of
249 surface ADAM17 compared to wt-iRhom2 (Fig. 3E).

250 These findings demonstrate the importance of the cytosolic iRhom2 N-terminus in regulating ADAM17
251 functions. They highlight the differential effects of TOC mutations and the cub deletion on iRhom2
252 function and their substantial impact on ADAM17 maturation, surface localisation and overall protein
253 levels. Overall, these findings suggest that the decrease in ADAM17 levels and downregulation of
254 surface ADAM17 seen in the cub deletion and to a lesser extent in the TOC site mutants occur in a
255 FRMD8-independent way. Importantly, the deletion of the TOC site in ndTOC shows a more severe
256 molecular phenotype than the TOC single point mutations. This is consistent with single point
257 mutations only partially disrupting TOC site functions, whereas a larger deletion has a more severe
258 effect.

259

260 **The iRhom2 N-terminus differentially regulates ADAM17-mediated shedding.**

261 Our findings that cub and TOC mutations decreases levels of mature ADAM17 is in line with recent *in*
262 *vivo* and *ex vivo* results (Siggs et al., 2014, Rabinowitsch et al., 2023). However, these findings are
263 counterintuitive to the earlier reported elevated ADAM17 shedding activity (Brooke et al., 2014, Hosur
264 et al., 2017, Hosur et al., 2018a, Hosur et al., 2018b). To analyse the effect of the N-terminus on
265 ADAM17 activity, we investigated the constitutive shedding of the ADAM17 substrates TGFα, IL1R2 and
266 AREG in HEK293 cells. As reported earlier, we found significantly increased substrate release with
267 additional expression of wt-iRhom2 compared to control cells (Fig. 4A,B)(Düsterhöft et al., 2021,
268 Kahveci-Türköz et al., 2023). Surprisingly, despite lower surface ADAM17 levels (Fig. 3D), ADAM17-
269 mediated shedding was not adversely affected in cells with N-terminal deletions nd197, cub and nd349
270 compared to control cells (Fig. 4A,B). In fact, shedding efficiency in cells with these deletions was

271 generally higher compared to shedding in control cells and comparable to cells expressing wt-iRhom2.
272 The largest deletion nd370 had the lowest ADAM17-mediated shedding, but was still comparable to
273 control cells (Fig. 4A,B).

274 To further examine the effects of large N-terminal deletions in iRhom2 on ADAM17-mediated shedding,
275 we used iRhom1- and iRhom2-deficient mouse embryonic fibroblasts (MEFs)(Christova et al., 2013).
276 These cells lack production of mature ADAM17, resulting in an absence of ADAM17-mediated
277 shedding. However, reintroduction of wt-iRhom2 expression effectively restored ADAM17-mediated
278 shedding (Fig. 4C). Surprisingly, constitutive ADAM17-mediated shedding was also restored for the N-
279 terminal deletions (nd197, cub and nd349), despite barely detectable amounts of mature ADAM17
280 present (Fig. S3D). However, the shedding activity restored by the N-terminal deletions was
281 significantly lower compared to cells expressing wt-iRhom2 (Fig. 4C). Interestingly, the largest deletion
282 (nd370), which lacked the third phosphorylation site, showed no restored shedding activity, similar to
283 control cells (Fig. 2G; Fig. 4C). Furthermore, we assessed ADAM17-mediated shedding stimulated by
284 the phorbol ester PMA (phorbol 12-myristate 13-acetate). While cells expressing wt-iRhom2 showed a
285 significant increase in shedding, this effect was not observed with iRhom2 deletion mutants (Fig. 4C).
286 This aligns with previous reports indicating that stimulated shedding is primarily driven by
287 phosphorylation at the described phosphorylation sites 1 and 2 (Cavadas et al., 2017, Grieve et al.,
288 2017), which are absent in all deletions (Fig. 2G).

289 In HEK293 cells, we further investigated the effects of the TOC mutations on AREG shedding.
290 Interestingly, additional expression of human wt-iRhom2 did not significantly increase constitutive
291 AREG shedding (Fig. 4D). This is consistent with our previous findings that overexpression of human
292 iRhom2 promotes shedding to a lesser extent than that of its mouse counterpart (Kahveci-Türköz et al.,
293 2023). Remarkably, iRhom2 has 96% sequence similarity (92% identity) in human and mouse, except
294 for a large insertion at the beginning of the N-terminus of human iRhom2 isoform 1, which was used
295 in this study (Fig. S3A). The discrepancy in shedding efficiency may be attributed to this dissimilarity.

296 Importantly, expression of the TOC mutations significantly increased shedding activity (Fig. 4D),
297 consistent with previous observations (Blaydon et al., 2012, Maney et al., 2015). Strikingly, we observed
298 even higher shedding efficiency with the complete TOC site deletion ndTOC (Fig. 4D), again showing a
299 more severe molecular phenotype than the single point mutations. Moreover, as expected, iRhom2
300 with TOC site mutations still promote PMA-stimulated ADAM17 shedding activity in iRhom1- and
301 iRhom2-deficient MEFs (Fig. 4E). However, the stimulated shedding activity of the TOC site mutants is
302 slightly but significantly reduced compared to wt-iRhom2, which is in line with reduced levels of mature
303 ADAM17 (Fig. 3C,E; Fig. 4E).

304 In summary, our results show that the N-terminus differentially regulates constitutive and stimulated
305 shedding and that the cub deletion loses the ability to promote stimulated ADAM17 activity.
306 Importantly, both larger N-terminal deletions and TOC mutations appear to lead to a reduction in
307 mature ADAM17 levels with concurrent higher constitutive ADAM17 activity.

308

309 N-terminal deletions of iRhom2 accelerate turn-over of mature ADAM17

310 To gain better insight into the molecular phenotypes of N-terminal iRhom2 mutations, we sought to
311 understand the underlying mechanisms. The observed decrease in mature ADAM17 levels can be
312 attributed to either an impaired maturation process or accelerated turnover leading to increased
313 internalisation of ADAM17 and its lysosomal degradation (Fig. 5A). Previous studies have shown that
314 destabilisation of the iRhom-ADAM17 complex by FRMD8 loss leads to increased lysosomal
315 degradation (Künzel et al., 2018, Oikonomidi et al., 2018). However, the effect we observed is FRMD8
316 independent and has not been studied before. To investigate whether the FRMD8-independent effect
317 of nd197 is due to accelerated degradation, we used the lysosomal inhibitors NH_4Cl and bafilomycin.
318 The use of these inhibitors for 8 h and 16 h rescued the levels of mature ADAM17 (Fig. 5B,C). After 16
319 h, the levels of mature ADAM17 in HEK293 cells expressing the cub or nd197 deletion reached those
320 of cells expressing wt-iRhom2 (Fig. 5C), indicating a similar maturation efficiency. Therefore,
321 accelerated turnover is likely the cause of the low mature ADAM17 levels when the deletions are
322 expressed. This is consistent with the reduced total levels of ADAM17 in cells expressing the deletions,
323 as maturation is still occurring, which depletes the pool of immature ADAM17, but the mature ADAM17
324 is not stable due to accelerated lysosomal degradation.

325 To further analyse the impact of the iRhom2 N-terminus on the turnover kinetic of ADAM17, we
326 performed a cycloheximide-based pulse-chase experiment (Fig. 5A). We observed a rapid decrease in
327 immature ADAM17 levels after inhibition of biosynthesis, as the maturation process continued and
328 subsequently immature ADAM17 levels declined until presumably no iRhom is left in the ER (Fig. 5D).
329 The presence of wt-iRhom2 facilitated this effect, significantly enhancing the reduction due to
330 increased ADAM17 transport to the Golgi and subsequent maturation. We found that nd197 and cub
331 deletions had the same effect (Fig. 5D), indicating that maturation process remained unaffected by the
332 N-terminal deletions.

333 Furthermore, the levels of mature ADAM17 decreased more rapidly in cells expressing the deletion
334 than in control cells or cells expressing wt-iRhom2 (Fig. 5D) indicating accelerated degradation of
335 mature ADAM17 in the presence of N-terminal deletions.

336 For comparison, we next studied the influence of TOC mutations on ADAM17 stability. 8 h of
337 bafilomycin-mediated lysosomal inhibition rescued the levels of mature ADAM17 in cells expressing

338 the TOC mutant to the same level as cells with wt-human iRhoms (Figure S3E). This suggests that the
339 same amount of mature ADAM17 is generated in cells expressing TOC mutants or wt-human iRhom2.
340 Lysosomal degradation of mature ADAM17 is slightly higher in cells with TOC mutations than in cells
341 expressing wt-iRhom2, resulting in slightly lower levels of total mature ADAM17 and less mature
342 ADAM17 on the cell surface, as described above (Figure 3C,E). However, this slightly accelerated
343 degradation does not seem to be strong enough to detect significant differences with the
344 cycloheximide-based pulse-chase experiments (Figure S3F).

345 Taken together, these results demonstrate the regulatory role of the N-terminus in controlling the
346 stability and turnover kinetics of mature ADAM17, but not immature ADAM17. In addition, the effects
347 of larger deletions are more severe compared to mutations or deletions at the TOC site, suggesting that
348 the stability of mature ADAM17 is only slightly affected by the TOC site, but is more dependent on the
349 interplay of other sites in the iRhom2 N-terminus. As there is no difference between nd197 and cub,
350 this mechanism appears to be FRMD8 independent.

351

352 **The iRhom2 N-terminal tail is a key determinant for regulating ADAM17 binding**

353 The interaction between iRhom and ADAM17 is a crucial requirement for their stability. Although the
354 transmembrane regions and extracellular domains are known determinants of the binding between
355 iRhom and ADAM17 (Cavadas et al., 2017, Grieve et al., 2017, Li et al., 2017, Düsterhöft et al., 2021,
356 Kahveci-Türköz et al., 2023), we nevertheless wondered whether the N-terminus could play a role in
357 this interaction. By co-immunoprecipitation, we analysed the binding between ADAM17 and iRhom2.
358 In both HEK293 cells and iRhom1- and iRhom2-deficient MEFs, we observed a significant decrease in
359 binding between ADAM17 and all deletions tested (nd197, cub, nd349 and nd370) compared to wt-
360 iRhom2 (Fig. 6A,B). However, the overall decrease in cellular ADAM17 levels could distort the results.
361 To address this issue, we engineered iRhom2 variants fused to the ER retention sequence KDEL, which
362 inhibits ADAM17 transport, maturation, and subsequent accelerated turnover of the iRhom2-ADAM17
363 complex (Fig. S4A) (Düsterhöft et al., 2021). In fact, even in this setting, we found a significant reduction
364 in ADAM17 binding for iRhom2 deletions compared to wt-iRhom2 (Fig. 6C; Fig. S4B). Interestingly, we
365 detected an additional significant reduction in ADAM17 binding for deletions larger than nd197,
366 indicating multiple regions in the N-terminus that regulate ADAM17 binding (Fig. 6A,C). This
367 observation is consistent with co-immunoprecipitation experiments using lysosomal inhibitors, where
368 inhibition of lysosomal degradation significantly increased the observable intact iRhom2-ADAM17
369 complex with nd197, but not with cub deletion (Fig. S4C). Under lysosomal inhibition, the precipitated
370 complexes with nd197 and cub showed increased amounts of mature ADAM17 indicating more rapid

371 degradation when in complex with these deletions (Fig. 6D,E). Importantly, we did not observe a
372 reduction in binding efficiency of the TOC site mutants (Fig. 6F).

373 In summary, our results clearly demonstrate the crucial role of the N-terminus for the binding affinity
374 between iRhom2 and ADAM17, which in turn influences the cohesion and stability of the iRhom2-
375 ADAM17 complex. Remarkably, there appear to be two parallel mechanisms regulating the ADAM17
376 interaction via the N-terminus: a clearly FRMD8-independent mechanism and a potential FRMD8-
377 dependent mechanism. Importantly, this ADAM17 interaction function is lost in the larger cub deletion
378 but not when only the TOC site is disrupted (Fig. 7).

379

380 **Discussion**

381 The iRhom2-ADAM17 sheddase complex is vital for both inflammatory signals (including TNFα release)
382 and EGFR signalling (via growth factor release such as AREG and TGFα). iRhom2 is a key regulator for
383 ADAM17's trafficking, maturation, activity, and stability. Understanding its regulation is crucial for the
384 molecular biology of ADAM17-associated diseases and subsequently for potential therapies targeting
385 these pathologies such as chronic inflammation and cancer pathologies including the autosomal
386 dominant inherited tylosis with oesophageal carcinoma (TOC). TOC is caused by so-called gain-of-
387 function mutations in the N-terminus of iRhom2, resulting in increased ADAM17-mediated shedding
388 and elevated AREG release. Mice with the cub (curly-bare) deletion exhibit a remarkably similar
389 phenotype to mice with TOC mutations, and both phenotypes can be rescued by knocking out
390 amphiregulin (Hosur et al., 2017, Hosur et al., 2018b). This suggests a shared molecular mechanism
391 between the large cub deletion and TOC single point mutations. However, studies on the cub deletion
392 have yielded conflicting findings regarding whether it has a positive or negative effect on ADAM17
393 shedding activity (Hosur et al., 2014, Siggs et al., 2014, Maney et al., 2015, Grieve et al., 2017). In
394 contrast, TOC mutations in iRhom2 clearly enhance ADAM17-mediated shedding (Blaydon et al., 2012,
395 Brooke et al., 2014), which is consistent with our results. In addition to TOC single point mutations, we
396 used a complete deletion of the TOC site, resulting in an even more pronounced effect. Our results
397 thus provide evidence for a loss of inhibitory function or loss of regulation by mutations at the TOC site
398 (Fig. 7). Notably, this site is also absent in the cub deletion, which should hence also lead to elevated
399 constitutive shedding activity of ADAM17. Here, it is crucial to consider the concurrent significant
400 decrease in mature ADAM17 levels when interpreting ADAM17 activity measurements. We could
401 demonstrate, that the cub deletion results in less mature ADAM17 that is, however, paradoxically
402 more active. This more complex molecular consequence of the large deletion in cub potentially
403 explains the previously contradictory studies. Importantly, a distinction must be made between
404 stimulated and constitutive ADAM17-mediated shedding. While the cub deletion and our other

405 designed deletions (nd197 and nd349) induce higher constitutive shedding activity of the available
406 surface ADAM17, stimulated shedding is completely abolished in all our deletions (Fig. 7). This is
407 consistent with the elimination of the first two crucial phosphorylation sites (Fig. 2F) (Cavadas et al.,
408 2017, Grieve et al., 2017). Intriguingly, the largest deletion nd370, which also lacks the third
409 phosphorylation site (Fig. 2F)(Cavadas et al., 2017, Grieve et al., 2017), additionally shows reduced
410 constitutive shedding. This is clear evidence of distinct signalling pathways that differentially regulate
411 constitutive and stimulated ADAM17 activity. Recent studies have highlighted the critical role of the
412 KRAS-ERK1/2 pathway in the shedding activity of the iRhom2-ADAM17 complex (Cavadas et al., 2017,
413 Grieve et al., 2017, Sieber et al., 2022). KRAS-G12 mutants in tumour cells harbouring iRhom2 with
414 TOC mutations further enhance constitutive ADAM17-mediated shedding (Sieber et al., 2022).
415 Interestingly, an ERK2 binding site was recently identified within the N-terminus upstream of
416 phosphorylation sites 1 and 2 (Fig. 2F)(Schumacher et al., 2023). Since this ERK2 interaction site is not
417 present in cub, it appears to be relevant for stimulated shedding rather than constitutive shedding.

418 Overall, the TOC site appears to serve as a regulatory interaction site with a restrictive effect on
419 ADAM17 activity. Consequently, we would classify TOC mutations, which disrupt this regulatory site,
420 as loss-of-regulation rather than gain-of-function. We hypothesise that both the cub deletion and the
421 TOC mutation lead to similar molecular consequences by disrupting the regulation of shedding activity.
422 However, the cub deletion results in additional more severe effects that partially obscure the increased
423 ADAM17 activity at the molecular level. Notably, the elevated constitutive shedding activity appears
424 to be the predominant and enduring molecular consequence observed *in vivo*, providing an
425 explanation for the strikingly similar phenotypes observed in TOC mice and cub mice (Hosur et al.,
426 2017, Hosur et al., 2018b).

427 The N-terminus of iRhoms emerges as a critical determinant for the stability of the iRhom-ADAM17
428 complex. This is again supported by our data and was recently also confirmed *in vivo*: mice with the
429 cub mutation show decreased ADAM17 levels in different tissues (Rabinowitsch et al., 2023). Recent
430 findings highlight the significance of FRMD8-binding in regulating iRhom stability and, consequently,
431 ADAM17 stability and functions (Künzel et al., 2018, Oikonomidi et al., 2018). While the loss of FRMD8
432 binding may contribute to the molecular consequences observed in cub deletions, our observations
433 demonstrate similar effects on mature ADAM17 stability in the nd197 deletion, which retains the
434 ability to bind FRMD8. This suggests that the N-terminus exerts a stabilising effect on the iRhom-
435 ADAM17 complex, largely independent of FRMD8: When these parts of the iRhom2 N-terminus, which
436 are not involved in FRMD8 binding, are deleted, accelerated turnover still occurs. Notably, TOC
437 mutants also exhibit a similar albeit less pronounced impact on stability of mature ADAM17.

438 Our study reveals that not only the transmembrane helix 1 and the IRHD, as previously described (Li et
439 al., 2017, Tang et al., 2020, Düsterhöft et al., 2021, Kahveci-Türköz et al., 2023), but also the iRhom2
440 N-terminus, directly contributes to ADAM17 binding. Through our ER-trapping approach, we have
441 demonstrated that the reduced binding of ADAM17 is not attributable to decreased ADAM17 levels.
442 Notably, the anterior half of the N-terminus (nd197) emerges as particularly crucial for efficient
443 ADAM17 interaction. However, larger deletions like the cub deletion (Δ268) result in an additional
444 significant reduction in binding efficiency, potentially mediated by FRMD8.

445 In summary, we postulate that while the binding affinity to ADAM17 is significantly reduced, iRhom2
446 N-terminal deletions such as cub retain the ability to bind immature ADAM17 in the ER, facilitating
447 efficient transport through the secretory pathway and normal maturation of ADAM17 (Fig. 7). During
448 maturation, the proteolytic removal of the ADAM17 prodomain may further decrease binding affinity,
449 as our recent study identified the prodomain as an additional binding determinant between the
450 ADAM17 ectodomain and the IRHD (Kahveci-Türköz et al., 2023). The reduced cohesion of the iRhom2-
451 matureADAM17 complex on the cell surface appears to induce instability and accelerated turnover,
452 culminating in lysosomal degradation (Fig. 7). Notably, the N-terminal deletions also elicit heightened
453 ADAM17 activity on the cell surface. Prior studies suggested that weakening the interaction between
454 ADAM17 and iRhom2, potentially induced by 14-3-3 binding at the phosphorylated N-terminus, could
455 trigger ADAM17-mediated shedding events (Cavadas et al., 2017, Grieve et al., 2017). Mutation or
456 deletion of the TOC site may enhance this effect on the surface leading to elevated activity and
457 weakening of the iRhom2-ADAM17 complex cohesion. This may also explain the difference in turn-
458 over kinetics between wt-iRhom2, cub and TOC. Since the complex cohesion of larger deletions such
459 as cub is already weakened, their turn-over and lysosomal degradation is much faster leading to a rapid
460 depletion of ADAM17.

461 In our study, we investigated the molecular consequences of N-terminal mutations in iRhom2 in order
462 to unravel the intricate regulatory system of the iRhom2-ADAM17 complex. It is important to
463 acknowledge that our investigation focused solely on these direct molecular mechanisms and did not
464 explore their integration within a more complex system. It is crucial to recognise that altered ADAM17
465 activity can initiate feedback loops that further modulate its own activity, including inducing ADAM17
466 activity by EGF receptor pathway activation (Grieve et al., 2017, Kubo et al., 2022, Sieber et al., 2022)
467 and the induction of gene expression of ADAM17, iRhoms, and other regulators through different
468 pathways including TNFα signalling (Arcidiacono et al., 2018, Babendreyer et al., 2020, Giese et al.,
469 2021, Kubo et al., 2022). Additionally, exogenous stimuli and cell stimulation by for example LPS can
470 also impact ADAM17 activity and the gene expression of iRhom2, ADAM17 and its substrates (Arndt
471 et al., 2011, McIlwain et al., 2012, Lu et al., 2017, Düsterhöft et al., 2021). Moreover, the N-terminus
472 can undergo cleavage and translocation into the nucleus, where it exerts incompletely understood

473 effects on gene expression (Dulloo et al., 2022, Zanotti et al., 2022). Furthermore, it is important to
474 consider that ADAM17 substrate specificity seems to be differentially regulated by iRhom1 and iRhom2
475 (Maretzky et al., 2013, Tang et al., 2020). Here, the N-terminal tail of iRhoms may also play a role.

476 Since the TOC mutations affect iRhom2, it is vital to note that high iRhom2 expression is often
477 predominantly associated with immune cells and inflammatory conditions. This role of iRhom2
478 becomes evident when considering that mice lacking iRhom2 exhibit a seemingly healthy phenotype
479 but display impaired immune responses (Adrain et al., 2012, Christova et al., 2013, Issuree et al., 2013).
480 Yet, the high iRhom2 gene expression we observed in keratinocytes underlines the significant role of
481 iRhom2 in skin homeostasis. This would be consistent with the TOC skin phenotype described earlier
482 (Fig. 7)(Blaydon et al., 2012, Brooke et al., 2014, Maney et al., 2015, Maruthappu et al., 2017).
483 Interestingly, the absence of iRhom2 activity in certain tissues in mice seems to be compensated by
484 the presence of iRhom1. Importantly, we observed that gene expression of both, iRhom2 and iRhom1,
485 is high in primary keratinocytes and skin tissue in mice and humans. Since mice with iRhom2 deficiency
486 show no obvious skin or hair phenotypes, iRhom1 seems to be able to largely compensate for iRhom2
487 deficiency in the skin as well. However, it was reported that iRhom2 deficient mice show reduced
488 epidermal thickness (Maruthappu et al., 2017). In contrast, the loss-of-regulation mutations do not
489 appear to be compensated for *in vivo*, highlighting their disruptive impact. Hence, the consistent
490 outcomes observed in mice with TOC and cub mutations as well as the predominant epithelial
491 symptoms of TOC patients indicate that elevated ADAM17 activity, particularly in epithelial cell types
492 such as keratinocytes, is the prevailing molecular consequence. Notably, in patients with TOC
493 mutations, tylosis manifests between the ages of 7 and puberty, while cancer develops much later in
494 life (Ellis et al., 2015), underscoring the cumulative effect of elevated constitutive ADAM17-mediated
495 shedding of EGF ligands over time. This is in line with our finding that disruption of the TOC site leads
496 to a gradual effect on iRhom2-ADAM17 complex functions: The larger deletion of the TOC site has a
497 stronger effect on ADAM17 activity than single point mutations. Furthermore, we found a significant
498 increase in iRhom2 and ADAM17 gene expression in oesophageal squamous cell carcinoma (OSCC)
499 compared to healthy oesophageal squamous tissue. This indicates that the iRhom2-ADAM17 complex
500 is a potential tumour marker for OSCC, which seems to be in line with the fact that patients with TOC
501 mutations, which increases ADAM17 activity, have a higher risk of developing OSCC (Fig. 7).

502 Overall, our results shed new light on the regulation of the iRhom2-ADAM17 complex by the
503 N-terminal tail of iRhom2. The intrinsically disordered nature of the N-terminus makes it an extensive
504 hub for protein binding and regulation. The molecular functions highlighted in our study warrant
505 further analysis and could potentially serve as viable targets for modulating ADAM17 activity. They
506 could offer promising avenues for combating ADAM17-associated pathologies such as cancer or
507 chronic inflammation.

508

509

510 **Methods**

511

512 *Bioinformatics*

513 Multiple sequence alignments were generated by utilising Clustal Omega (Sievers et al., 2011).
514 Secondary structure prediction and analysis of intrinsically disordered regions were done with IUPred3
515 (Meszaros et al., 2009, Erdos et al., 2021), NetSurfP-2.0 (Klausen et al., 2019) and ANCHOR2 (Dosztanyi
516 et al., 2009, Meszaros et al., 2009, Meszaros et al., 2018). The following sequences were used
517 (UniProtKB entries): Q6PJF5 (human iRhom2) and Q80WQ6 (murine iRhom2). Nuclear localisation
518 sequence analysis was performed with NLStraddamus (Nguyen Ba et al., 2009).

519 *Ab initio* structure prediction of cytosolic iRhom2 N-terminus was done with AlphaFold2 (Jumper et al.,
520 2021) utilising ColabFold (Mirdita et al., 2022). Structural modelling using the deep learning algorithm
521 AlphaFold2 was done without homology templates. MMseq2 was used as the multiple sequence
522 alignment. The structural modelling went through 12 iterations. The respective top-ranked models
523 were used.

524 To identify conserved sequence regions, the tool CONYAR (Conserved You Are) was employed to
525 perform high-throughput comparison of as many sequences of a target protein as possible (Kahveci-
526 Türköz et al., 2023).

527

528 *In silico gene expression analysis*

529 We accessed Affymetrix Human Genome U133 Plus 2.0 Array platform data from public repositories,
530 curated by the GENEVESTIGATOR platform (Immunai, USA)(Hruz et al., 2008). The GENEVESTIGATOR
531 software was utilised for gene expression meta-analysis of indicated genes in various tissues, biopsies,
532 and primary cells (assessed on 20 May 2023). To analyse gene expression patterns under physiological
533 conditions, only samples from healthy and untreated tissues were included. Similarly, for assessing
534 baseline gene expression in cancerous tissue, only untreated samples were considered.

535 List of used experiment IDs for indicated tissue and primary cells: a) murine heart: MM-00170 (Muchir
536 et al., 2007), MM-00253 (Dufour et al., 2007), MM-00257 (Zhao et al., 2007), MM-00262 (Alcendor et
537 al., 2007), MM-00300 (Ramchandran et al., 2006), MM-00322, (Thorrez et al., 2008), MM-00330 (Lattin
538 et al., 2008), MM-00368 (Barger et al., 2008), MM-00384 (Wong et al., 2010), MM-00476 (Abd Alla et
539 al., 2016), MM-00485 (Oka et al., 2011), MM-00492 (Wang et al., 2016), MM-00497 (Shuai et al., 2011),
540 MM-00507 (Shuai et al., 2011), MM-00561 (Ricard et al., 2010), MM-00834 (Traister et al., 2013), MM-
541 00841 (Mercader et al., 2012), MM-01538 (Gambino et al., 2013), MM-01642 (Lucas et al., 2014), MM-
542 01875 (Lucas et al., 2014); b) murine primary fibroblast (dermis): MM-00159 (Vallender and Lahn,

543 2006), MM-00180 (Vallender and Lahn, 2006), MM-00627 (Garinis et al., 2009), MM-00724 (Garinis et
544 al., 2009); c) murine primary keratinocytes: MM-01215 (Allende et al., 2013); d) healthy human
545 epidermis tissue (biopsy): HS-02924 (Esaki et al., 2015); e) human primary keratinocytes (untreated):
546 HS-02625 (Yunoki et al., 2018), HS-02787 (Busch et al., 2008), HS-02490 (Swindell et al., 2012), HS-
547 00220 (Sa et al., 2007); f) human primary keratinocytes (treated with TNFα, IFNα, IFNγ or IL4; 24 h):
548 HS-02490 (Swindell et al., 2012); g) human primary keratinocytes (treated with 10 ng/ml I IFNγ; 96 h):
549 HS-02625 (Yunoki et al., 2018); h) human primary fibroblasts (untreated): HS-00393, HS-00481 (Chen
550 et al., 2008), HS-00805 (Verkerk et al., 2009), HS-00928 (Wang et al., 2012), HS-00963, HS-00989
551 (Strunnikova et al., 2009), HS-01109 (Visser et al., 2012), HS-01279 (Marchina et al., 2014), HS-01311
552 (Henrichsen et al., 2011), HS-01326 (Voets et al., 2012), HS-02421 (Smith et al., 2008); i) primary artery
553 smooth muscle cells (heart): HS-00478 (Shalhoub et al., 2010); j) primary bronchial smooth muscle
554 cells: HS-00039 (Bosse et al., 2007); k) healthy oesophagus squamous tissue (biopsy): HS-01298 (Wang
555 et al., 2013), HS-00217, HS-00017 (Roth et al., 2006), HS-01525 (Sato et al., 2013); squamous cell
556 carcinoma (grade G1): HS-01298 (Wang et al., 2013); oesophagus adenocarcinoma: HS-00002; HS-
557 01298 (Wang et al., 2013); Barrett´s oesophagus (pre-malignant): HS-01298 (Wang et al., 2013);
558 primary macrophages: HS-01265; primary granulocytes: HS-00250; primary leukocytes: HS-00261;
559 primary monocytes: HS-01403.

560

561 *Cloning*

562 The cloning procedures were performed as previously described (Düsterhöft et al., 2021): NEBuilder
563 HiFi DNA Assembly Master Mix (NEB, E2621L) was utilised to produce different plasmids with the
564 desired inserts according to the manufacturer's instructions. All iRhom constructs were cloned into the
565 pMOWS backbone (Ketteler et al., 2002, Düsterhöft et al., 2021). Site-directed mutagenesis was
566 performed using overlapping PCR (Ho et al., 1989).

567

568 *Cell culture*

569 All cells were cultured in a humidified incubator at 37 °C, 5% CO_2 in DMEM10% (unless otherwise
570 indicated). DMEM10% consists of DMEM high-glucose (Sigma-Aldrich) supplemented with 10% foetal
571 calf serum (PanBiotech), 100 mg/l streptomycin (Sigma-Aldrich) and 60 mg/l penicillin (Sigma-Aldrich).
572 Production of stable cell lines was done as described before (Düsterhöft et al., 2021). MEFs double
573 deficient for iRhom1 and iRhom2 were obtained from indicated mouse lines as described before
574 (Christova et al., 2013, Düsterhöft et al., 2021). HEK293 cells were purchased from German Collection
575 of Microorganisms and Cell Cultures (GmbH DSMZ- No. ACC 305). Normal human epidermal
576 keratinocytes and human dermal fibroblasts were isolated from human skin samples as described

577 before (Schmitt et al., 2018). Primary keratinocytes were cultivated in Dermalife K – Life Line (Cell
578 Systems LL-0007). Primary fibroblasts were cultivated in DMEM10%.

579

580 *Quantitative PCR (RT-qPCR)*

581 mRNA expression levels were measured by quantitative PCR and normalised to the mRNA expression
582 levels of the selected reference genes. Cytochrome c1 (CYC1) and ribosomal protein L13a (RPL13A)
583 were chosen as the most stable reference genes based on the results from the CFX Maestro Software
584 1.1 (Bio-Rad). RNA was extracted using RNeasy Kit (Qiagen) and quantified photometrically (NanoDrop,
585 Peqlab, Erlangen, Germany). For reverse transcription, the PrimeScriptTM RT Reagent Kit (Takara Bio
586 Europe) was used, according to the manufacturer's protocol. PCR reactions were performed in
587 duplicates of 10 µl volume comprising 1 µl of cDNA template, 5 µl iTaq Universal SYBR Green Supermix
588 (Bio-Rad), 3 µl H_2O and 0.5 µl forward and reverse primer. The following primers were used with the
589 primer annealing time given in brackets: CYC1 (forward: AGC TAT CCG TGG TCT CAC C, reverse: CCG CAT
590 GAA CAT CTC CCC ATC; 59 °C), RHBDF1 (forward: GAC AGC CCA CAT CTC TTC AC , reverse: TCC TTG CTC
591 ACT CCA AAC CA; 56 °C), RHBDF2 (forward: CGA TTG ACC TGA TCC ACC, reverse: CAA AGT CTC CGA GCA
592 GTC C; 58 °C) and RPL13A (forward: GCC CTA CGA CAA GAA AAG CG, reverse: TAC TTC CAG CCA ACC
593 TCG TGA; 60 °C). All RT-qPCR reactions were performed on a CFX Connect Real-Time PCR Detection
594 System (Bio-Rad) using the following protocol: 40 cycles of 10 s denaturation at 95 °C, followed by 10 s
595 annealing at the corresponding temperatures and 15 s amplification at 72 °C. PCR efficiency was
596 calculated from the uncorrected RFU values using LinRegPCR version 2020.0 (Ruijter et al., 2009). CFX
597 Maestro Software 1.1 (Bio-Rad) was used for relative quantification.

598

599 *Co-immunoprecipitation and enrichment of glycosylated proteins*

600 Precipitation experiments were done as described before (Düsterhöft et al., 2021, Kahveci-Türköz et
601 al., 2023): Cells were lysed in 1 ml lysis buffer (50 mM Tris, 2 mM $CaCl_2$, 137 mM NaCl, 2 mM EDTA,
602 10 mM 1,10-Phenanthroline, pH 7.5) supplemented with cOmplete™ protease inhibitor (Sigma;
603 11697498001). The lysates were cleared by centrifugation at 16,000 x g for 20 minutes at 4 °C. For the
604 enrichment of glycosylated proteins, 450 µl of cleared lysate was incubated with 30 µl of Concanavalin
605 A sepharose (Sigma; C9017). For co-immunoprecipitations (coIPs), 450 µl of cleared lysate was
606 incubated with 10 µl of anti-HA magnetic beads (Thermo; 88836). The lysates were incubated with the
607 beads for 90 min. Afterwards, the beads were washed five times with lysis buffer. The beads were
608 heated in 40 µl reducing loading buffer (3% SDS, 16% glycerol, 8% 2-mercaptoethanol, 0.01%
609 bromophenol blue, 0.1 M Tris HCl, pH 6.8) at 65 °C for 20 minutes.

610

611 *Western blotting*

612 Samples were subjected to SDS-PAGE and transferred onto PVDF membranes (Millipore, Immobilon-
613 FL). Membranes were blocked with 5% non-fat dry milk in TBS (50 mM Tris, 150 mM NaCl, pH 7.4) for
614 20 min at room temperature. Primary antibodies were incubated overnight at 4 °C in 0.1% Tween-TBS
615 and 1% BSA. After three washes with 0.1% Tween-TBS, membranes were incubated with secondary
616 antibody for 1 h at room temperature. Additional washing steps included one wash with 0.1% Tween-
617 TBS and three washes with TBS. Protein detection was performed using the Odyssey 9120 imager
618 system (LI-COR) and the ChemiDoc MP Imaging System (Bio-Rad). Band intensities were quantified
619 using Image Studio Lite software (LI-COR). The following primary antibodies were used: αADAM17
620 (1:1000; Abcam; ab39162), αHA (1:2000; Biolegend; 901502), αTransferrin-receptor (1:2000; Thermo,
621 H68.4, 13-6800), αGAPDH (1:2000; Thermo, GA1R, 15738), αiRhom2 (1:1000; R&D; 996308;
622 MAB10048). The following secondary antibodies were used at the indicated dilutions: DyLight-680-
623 conjugated αmouse (1:20000; Thermo; 35519), DyLight-800-conjugated αrabbit (1:20000; Thermo;
624 35571), HRP-conjugated goat αmouse and αrabbit (1:20000; Jackson ImmunoResearch Laboratories,
625 Inc).

626

627 *Shedding activity - AP-Assay*

628 ADAM17-mediated shedding activity was measured by an alkaline phosphatase (AP)–based assay as
629 described before (Düsterhöft et al., 2021, Kahveci-Türköz et al., 2023). In brief, we used cells transfected
630 with ADAM17 substrates fused to an alkaline phosphatase to analyse shedding activity: The following
631 ADAM17 substrates cloned in pCndA3.1 were utilised: AP-IL1R2, AP-TNFα, AP-AREG. HEK293 cells
632 stably expressing the indicated iRhom2 constructs were transiently transfected with the indicated
633 substrate. In the case of MEFs, the indicated iRhom2 construct combined with the indicated substrate
634 was transiently transfected. Shedding activity was assessed under different conditions: either the
635 metalloprotease inhibitors marimastat (broad-spectrum, 10 µM) (Sigma; M2699) or TAPI1 (ADAM17
636 preferential inhibitor, 10 µM) (Sigma; SML0739) were used. When indicated, cells were stimulated with
637 100 nM PMA (Sigma; P1585). DMSO served as the vehicle control. Following treatment, cells were
638 incubated: 90 min (AREG, TGFα), 120 min (IL1R2), or 240 min (AREG) at 37 °C. To evaluate proteolytic
639 activity of ADAM17, we measured alkaline phosphatase (AP) activity in both the supernatant and cell
640 lysates (lysis buffer: 50 mM Tris, 137 mM NaCl, 2 mM EDTA, 10 mM 1,10-phenanthroline, pH 7.5,
641 supplemented with cOmplete™ protease inhibitor). By continuously measuring AP activity at 405 nm
642 using the FLUOstar Optima (BMG LABTECH) after adding a p-nitrophenyl phosphate (PNPP) solution
643 (Thermo; 37620), we calculated the slope representing the change in absorbance at 405 nm per min.

644 ADAM17 activity was determined by calculating the PNPP substrate turnover (AP activity) in the
645 supernatant relative to the total turnover in the supernatant plus cell lysate.

646

647 *Flow cytometric analysis*

648 The staining process was conducted using PBS with 0.2% BSA as the assay buffer, and all steps were
649 carried out at 4 °C or on ice. A total of $2x10^5$ cells of interest were incubated with the primary antibody
650 for 1 h. Subsequently, cells were washed twice with 400 µl of assay buffer. The secondary antibody was
651 added, and cells were incubated in the dark for 45 mins. Following two additional washing steps, the
652 fluorescence signal was assessed using flow cytometry (LSRFortessa, BD Biosciences, Heidelberg,
653 Germany), and FlowJo V10 software was employed for data analysis. The geometric mean of
654 fluorescence intensity was determined to assess cell surface localisation. The primary antibodies used,
655 along with their dilutions, were as follows: αADAM17 (1:100; R&D Systems; MAB 9301), αHA (1:500;
656 Biolegend; 901502). The secondary antibody used was Allophycocyanin-conjugated αmouse (1:200;
657 Jackson ImmunoResearch; 115-135-164).

658

659 *Lysosomal inhibition*

660 Cell cultures were first grown to approximately 80% confluence. Cells were treated with either
661 bafilomycin A1 (B) or NH_4Cl (N). An untreated control was also included using DMSO as a vehicle
662 control. The cells were then incubated for 8 h (B: 0.1 µM; N: 20 mM) or 16 h (B: 0.5 µM; N: 40 mM).
663 After incubation, the plates were placed on ice and the medium was discarded. The cells were washed
664 once with PBS and then harvested with 1 ml cold PBS. A 10 µl aliquot was taken from the cell suspension
665 to determine the number of cells for sample adjustment. The harvested cells were centrifuged at
666 1000 g for 5 min at 4°C and the supernatant was discarded. Cell pellets were used for lysis and coIPs
667 followed by Western blotting as described above.

668

669 *Cycloheximide-based pulse chase experiment*

670 Cell cultures were used at approximately 80% confluence. Cells were incubated with cycloheximide
671 (10 µg/ml) for 3 or 6 h. After washing with PBS, the cells were harvested in 1 ml cold PBS and a 10 µl
672 aliquot was taken from the cell suspension to determine the number of cells for sample adjustment.
673 Harvested cells were pelleted and used for lysis followed by Western blotting as described above.

674

675 *Statistics*

676 Statistic was done as described before (Düsterhöft et al., 2021): Experiments were repeated at least
677 three times, as indicated in the figure legends. Quantitative data are presented as mean with standard
678 deviation (SD). Statistical analysis was performed using the generalised mixed model analysis (PROC
679 GLIMMIX, SAS 9.4, SAS Institute Inc., Cary, North Carolina, USA), assuming normal, lognormal, or beta
680 distribution, with the day of the experiment considered as a random factor to assess treatment effect
681 differences across the results. Diagnostic tests, including residual analysis and the Shapiro-Wilk test,
682 were utilized. In cases of heteroscedasticity (as determined by the covtest statement), degrees of
683 freedom were adjusted using the Kenward-Roger approximation. All p-values were adjusted for
684 multiple comparisons using the false discovery rate (FDR). Statistical significance was defined as
685 $p < 0.05$, with the following notation: p: * < 0.05, ** < 0.01, *** < 0.001.

686

687 **Declarations**

688

689 **Ethics approval**

690 This study was conducted according to the principles of the Declaration of Helsinki and approved by
691 the ethics committee of the Medical Faculty RWTH Aachen, Germany (EK 188/14).

692

693 **Authors' contribution**

694 S.D. conceived, designed, and coordinated the study and wrote the manuscript. S.D. and A.L. analysed
695 data and revised the manuscript. S.D., K.B., L.L., S.K.T., C.F., F.S., S.K., D.K., C.G, N.T. and X.G. performed
696 experiments and analysed the results. S.D. conducted protein bioinformatics analysis and structure
697 prediction. A.B. developed the algorithm for high-throughput identification of conserved regions and
698 performed conservation analysis. S.D. and S.K. performed meta-analysis of *in vivo* and *ex vivo* datasets.
699 C.A. generated FRMD8/iTAP knock-out cells. S.H. and J.M.B. isolated primary keratinocytes and
700 fibroblasts. All authors read and approved the final version of the manuscript.

701

702 **Funding**

703 To S.D. Research Fellowship of the German Research Foundation (280679981), ERS Start-up
704 (StUpPD_299-18) and two START grants (#691903-06/19 and #692305- 06/23) of the Medical Faculty
705 of the RWTH Aachen University. To A.L. funding from the German Research Foundation (418426903)
706 and from the Interdisciplinary Centre for Clinical Research (IZKF) Aachen (A-1-5).

707

708 **Conflict of interests**

709 The authors have no relevant financial or non-financial interests to disclose.

710

711 **Abbreviations**

712 a disintegrin and metalloproteinases (ADAM); amphiregulin (AREG); co-Immunoprecipitation (coIP);
713 epidermal growth factor receptor (EGFR); FRMD8 (FERM Domain Containing 8), interferon (IFN);
714 interleukin (IL); interleukin 1 receptor 2 (IL1R2); iRhom homology domain (IRHD); oesophageal cancer
715 (OC); oesophageal adenocarcinoma (OAC); oesophageal squamous cell carcinoma (OSCC); predicted
716 aligned error (PAE); predicted local distance difference test (pLDDT); transforming growth factor alpha
717 (TGFα); tumour necrosis factor alpha (TNFα)

718

719 **Acknowledgment**

720 We thank Johanna Jakob for cultivation of the primary cells.

721

722 **Figure legends**

723 **Figure 1:iRhom2 gene expression is high in skin and OSCC (A)** Structurally, iRhoms have a distinct
724 topology composed of a rhomboid core with seven transmembrane helices (TMH). The extracellular
725 iRhom homology domain (IRHD) is situated between TMH1 and TMH2. Additionally, iRhoms possess a
726 large cytosolic N-terminal tail: 375 residues in murine iRhom2 and 403 residues in human iRhom2.
727 Relative positions of key characteristics are labelled for murine iRhom2: (1) putative FRMD8 binding
728 site; (2) TOC mutation site - in human iRhom2: I186T (murine position: 156)(Blaydon et al., 2012),
729 D188N (murine position: 158)(Blaydon et al., 2012), D188Y (murine position: 158)(Mokoena et al.,
730 2018), P189L (murine position: 159)(Blaydon et al., 2012), R197S (murine position: 167)(Qu et al.,
731 2019); (3) phosphorylation sites and putative 14-3-3 binding sites. **(B)** Role of iRhoms in ADAM17
732 biology: iRhoms regulate ADAM17 by binding to immature proADAM17 in the ER and transporting it
733 to the Golgi for maturation. The inhibitory prodomain is then proteolytically removed by furin-like
734 proteases. This process allows mature ADAM17 in complex with iRhoms to localise to the cell surface
735 and initiate shedding of its substrates, enabling various pathways including TNFα and EGFR signalling.
736 **(C)** Curated Affymetrix Human Genome U133 Plus 2.0 Array platform data from public repositories
737 (Hruz et al., 2008) were assessed with the GENEVESTIGATOR software. The GENEVESTIGATOR platform
738 allows for the comparison of mRNA expression of genes between samples of different experimental
739 data sets: Gene expression levels of iRhom1 (RHBDF1) and iRhom2 (RHBDF2) from healthy human
740 epidermis tissue (n = 10), untreated primary human keratinocytes from healthy tissue (n = 13),

untreated primary human fibroblasts from healthy dermis tissue (n = 57), untreated primary human artery smooth muscle cells from healthy heart tissue (n = 10), untreated primary human bronchial smooth muscle cells from healthy heart tissue (n = 10) were analysed. To compare the gene expression levels of iRhom1 and iRhom2 in one sample, the iRhom2/iRhom1 ratio was calculate for each sample. **(D)** Immunoblot of cell lysates from primary keratinocytes or primary fibroblasts. n = 3. **(E)** RT-qPCR of primary keratinocytes and primary fibroblasts. n = 3. **(F-G)** Data from curated Affymetrix Human Genome U133 Plus 2.0 Array platform data as described in (C): **(F)** Gene expression levels of iRhom1 and iRhom2 in primary keratinocytes from healthy tissue treated with: untreated control (n = 13) or treated for 24 h with indicated proinflammatory stimulants (n = 3) or treated for 96 h with IFNγ (n = 2). **(G)** Gene expression levels of iRhom1 and iRhom2 in healthy human oesophagus squamous tissue (n = 23) compared to expression levels in human oesophageal squamous cell carcinoma (OSCC; n = 8), human oesophageal adenocarcinoma (OAC; n = 26) and Barrett´s oesophagus (n = 17).

Figure 2: The cytosolic N-terminal tail of iRhom2 is an intrinsic disordered hub for regulation and differentially controls levels of mature ADAM17. (A) Using IUPred3 (Meszaros et al., 2009, Erdos et al., 2021) and NetSurfP-2.0 (Klausen et al., 2019) , we assessed the probability of disordered regions and the presence of different structural elements in the cytosolic N-terminus of murine and human iRhom2 (residue 1 to 375). IUPred3 score describes the probability of disordered regions. NetSurfP-2.0 output gives the probability of the presence of disorder, alpha-helices, and beta-sheets. **(B)** *Ab initio* structural modelling of the N-terminus of murine iRhom2 using the deep learning algorithm AlphaFold2. Best ranked model is depicted in cartoon representation coloured according to pLDDT (predicted local distance difference test in [%]) score. **(C)** Consistent with (A), the structural prediction of the N-terminus of murine and human iRhom2 using AlphaFold2 demonstrates only small locally structured regions: Hence the iRhom2 N-terminus is largely disordered, as indicated by the overall low average pLDDT score per sequence position of the five predicted, ranked models. **(D)** The predicted align error (PAE) of the best ranked structural models support this finding: the individual amino acid residues in the disordered/unstructured N-terminus are largely not fixed in their position relative to each other and therefore have a high spatial uncertainty (20 - 30 Å). **(E)** Using the bioinformatic tools IUPred3 and ANCHOR2 (Mészáros et al. 2009) putative binding sites within the cytoplasmic N-terminus of human iRhom2 were identified. The plots show the calculated probability for an amino acid residue to be part of a binding site. Regions above 50% probability (ANCHOR2) and with a certain length are putative binding sites such as the highly conserved region which harbours all known TOC mutations. Our designed TOC site deletion ndTOC comprises the three main TOC mutations, but not the newest identified R197S (Qu et al., 2019). **(F)** We used the algorithm CONYAR (Kahveci-Türköz et al., 2023) to retrieve all available amino acid sequences of iRhom1 and iRhom2 from UniProtKB and compare them

776 to identify highly conserved regions within the amino acid sequences of that gene. In the case of
777 iRhom2 (query: RHBDF2) sequences from 381 species and in case of iRhom1 (query: RHBDF1)
778 sequences of 301 species were extracted. The TOC site was identified by CONYAR as a highly conserved
779 region and its conservation is shown as WebLogo representation. Asterisks indicate the positions of the
780 natural occurring TOC mutations in human iRhom2. M indicates the position of arginine methylation
781 found by high throughput proteomics (Hornbeck et al., 2015). **(G)** Overview of the relative position of
782 key regulatory sites and binding interfaces in wt-iRhom2 and in our designed N-terminal deletions.
783 Phosphorylation sites (P1, P2 and P3) are binding sites for 14-3-3 proteins. NLS: predicted nuclear
784 localisation sequence. **(H,I)** To analyse binding between iRhom2 constructs and endogenous FRMD8,
785 coIPs were performed using the indicated iRhom2 constructs (with HA tag) as bait. HEK293 cells stably
786 expressing the indicated murine iRhom2 deletions (H) or human iRhom2 constructs (I) as well as GFP
787 (ctr.) as negative control were used. At around 55 kDa the shorter fragment of cleaved iRhom2 (siR2)
788 as reported before (Adrain et al., 2012, Christova et al., 2013) is visible. This fragment was described
789 as consequence of cleavage by signal peptidase complex (Dulloo et al., 2022, Zanotti et al., 2022) but
790 may additionally occur as artefact after lysis as we detect inconsistent amounts of the small fragment
791 in different experiments. n = 4.

792

793 **Figure 3: The iRhom2 N-terminus regulates levels of mature ADAM17. (A)-(C)** Immunoblot of samples
794 from HEK293 cells stably expressing the indicated murine iRhom2 variants (A,B) or human iRhom2
795 variants (C) as well as GFP (ctr.) as negative control. Glycosylated proteins from cell lysates were
796 enriched with concanavalin A beads. HEK293 cells have endogenous iRhoms and therefore exhibit a
797 basal level of ADAM17 maturation. The maturation level of ADAM17 can be detected by the presence
798 of mature ADAM17 with lower molecular weight than immature ADAM17 (imA17). ADAM17
799 maturation was assessed by densitometric measurements and calculation of the ratio between mature
800 ADAM17 and immature ADAM17. Total ADAM17 levels were assessed by densitometric
801 measurements and calculation of the ratio between total ADAM17 (mature plus immature ADAM17)
802 divided by the respective input control. Values were normalised to the respective wt-iRhom2 sample.
803 n > 4. **(D)-(E)** Levels of surface ADAM17 in cells stably expressing indicated murine iRhom2 constructs
804 (D) or human iRhom2 constructs (E) were measured by flow cytometry. For quantification, the
805 geometric mean of the specific fluorescence signal was determined and normalised to the respective
806 wt-iRhom2. n > 4.

807

808 **Figure 4: N-terminal mutations in iRhom2 dysregulate ADAM17-mediated shedding. (A-E)**
809 Constitutive ADAM17-mediated shedding activity was assessed by performing an alkaline phosphatase

810 (AP) assay in HEK293 cells (A,B,D) and MEFs deficient for iRhom1 and iRhom2 (C,E) expressing the
811 indicated iRhom2 constructs. The ADAM17 substrate TGFα, IL1R2 or AREG tagged with AP were used.
812 The metalloprotease inhibitors marimastat (10 µM) or the more ADAM17 specific inhibitor TAPI1
813 (10 µM) were used as negative control. Where indicated, ADAM17 activity was additionally stimulated
814 by the phorbol ester PMA (100 nM). n > 4.

815

816 **Figure 5: The N-terminal tail of iRhom2 regulates protein turn-over kinetics. (A)** After biosynthesis in
817 the ER, ADAM17 is transported to the Golgi for maturation with the help of iRhoms. The complex of
818 mature ADAM17 and iRhom is transported to the cell surface. After internalisation, the complex is
819 degraded in the lysosomes. Like all ER proteins, to a certain extent immature ADAM17 can be
820 transported directly to the lysosome by ER-phagy. **(B-C)** To analyse the fate of mature ADAM17 in cells
821 expressing the nd197 and cub deletion, cells were treated with either NH_4Cl ("N") or bafilomycin ("B")
822 for 8 h (B) or 16 h (C) to inhibit lysosomal degradation. Levels of mature ADAM17 were assessed by
823 densitometric measurements and calculation of the ratio between mature ADAM17 and the loading
824 control GAPDH, which is independent of lysosomal degradation. (n = 4) **(D)** To assess the turn-over rate
825 of ADAM17 a cycloheximide-based (Chx) pulse-chase experiment was performed. Reduction of
826 ADAM17 levels was assessed by densitometric measurements and normalisation to 0 h Chx treatment
827 (set to 1). (n = 3).

828

829 **Figure 6: The N-terminus of iRhom2 regulates ADAM17 interaction.** To analyse interaction between
830 ADAM17 and the indicated murine iRhom2 variants, coIPs were performed using the iRhom variants
831 (with HA tag) as bait. Immunoblotting and subsequent densitometric measurements were used to
832 quantitatively analyse iRhom2-ADAM17 binding (ratio of co-precipitated ADAM17 and precipitated
833 iRhom2) and normalised to wt-iRhom2. **(A)** HEK293 stably expressing indicated iRhom2 variants or GFP
834 (ctr.) were used (n > 17). **(B)** MEFs from mice deficient for iRhom1 and iRhom2 stably expressing
835 indicated iRhom2 variants or GFP (ctr.) were used (n = 4). **(C)** HEK293 expressing indicated iRhom2
836 variants or GFP (ctr.) fused to the ER-retention motif KDEL were used (n > 5). **(D) – (E)** To analyse the
837 fate of mature ADAM17 specifically in the iRhom2-matureADAM17 complex containing either the
838 nd197 deletion, cub deletion or wt-iRhom2, cells were treated with either 40 mM NH4Cl (N) or 500 nM
839 bafilomycin (B) for 8 h or 16 h to inhibit lysosomal degradation. Maturation levels of bound ADAM17
840 was assessed by densitometric measurements and calculation of the ratio between mature ADAM17
841 and immature ADAM17. The quantitative analysis of ADAM17 binding can be found in Fig. S4C. (n = 4).
842 **(F)** HEK293 stably expressing indicated human iRhom2 variants or GFP (ctr.) were used for coIP
843 experiments as describe above. (n > 4).

844

845 **Figure 7: The iRhom2 N-terminal tail regulates ADAM17 binding and shedding activity.** Wt-iRhom2
846 plays a critical role in the transport, maturation and shedding activity of ADAM17, ensuring the proper
847 regulation of downstream signalling pathways such as EGFR activation. Conversely, disruptions of the
848 TOC site in the N-terminal tail of iRhom2 lead to dysregulated higher constitutive shedding activity (loss
849 of regulation mutation). This increased activity of the iRhom2-ADAM17 complex may also be the cause
850 for the accelerated ADAM17 turnover observed for TOC site mutations. The elevated release of EGF
851 receptor ligands such as AREG in iRhom2 high-expressing keratinocytes contributes to an amplified
852 EGFR signalling, resulting in the well-described hyperkeratosis seen in TOC patients. The higher risk for
853 OSCC, which also shows higher iRhom2 and ADAM17 expression, may also be attributed to this
854 phenomenon. In the case of the cub deletion, not only is the TOC site disrupted, but efficient binding
855 to ADAM17 is also impaired, further accelerating ADAM17 turnover and lysosomal degradation.
856 Furthermore, the cub deletion loses the ability to promote stimulated ADAM17 shedding activity.
857 These molecular consequences are independent of FRMD8 and are regulated by the first 200 residues
858 of the N-terminal tail.

859

860

861 **Figure S1: (A)** Gene expression levels of iRhom1 (RHBDF1) and iRhom2 (RHBDF2) (see Fig. 6A) from
862 primary cell samples are shown as stacked bars, indicating that total iRhom (iRhom1 plus iRhom2)
863 expression may be regulated to a similar overall level in untreated primary cells from healthy tissue.
864 **(B)** Gene expression levels of iRhom1 (RHBDF1) and iRhom2 (RHBDF2) from untreated primary murine
865 keratinocytes from healthy tissue (n = 5), untreated primary murine fibroblasts from healthy dermis
866 tissue (n = 12) and samples from healthy murine heart tissue (n = 98) were analysed. **(C)** Gene
867 expression levels of ADAM17, AREG, TGFα, TNFα and IL6 were analysed in oesophagus and cancerous
868 oesophagus tissues (see Fig. 6C). **(D)** To test whether the increased iRhom2 expression levels were due
869 to the presence of macrophages or monocytes in the samples, the ratio between iRhom2 and CD14
870 (monocyte and macrophage markers) of the samples was calculated and compared with the values of
871 the indicated immune cell populations (Fig. S2), showing that the measured high iRhom2 levels cannot
872 be explained by the presence of immune cells.**(E)** Gene expression levels of iRhom1 (RHBDF1) and
873 iRhom2 (RHBDF2) fromHEK293 cells (n = 6).

874

875 **Figure S2:** Gene expression levels of indicated immune cell markers: CD94 (NK-cells), CD3γ (T-cells),
876 CD19 (B-cells), CD64 (monocytes/macrophages, Dendritic cells), CD14 (monocytes/macrophages,
877 granulocytes), CD66b/CD67 (granulocytes), CD170 (tumour-associated neutrophiles,

878 monocytes/macrophages, activated dendritic cells, lymphocytes-subsets) were analysed with the
879 GENEVESTIGATOR platform **(A)** in oesophagus and cancerous oesophagus tissues (see Fig. 1G) and **(B)**
880 in indicated human immune cell populations: macrophages (n = 6), granulocytes (n = 6), leukocytes
881 (n = 8) and monocytes (n = 13).

882

883 **Figure S3: (A)** Protein sequence alignment of the N-terminal region of the cytosolic tail of human
884 iRhom2 (isoform 1 and isoform 2) and murine iRhom2. **(B)** Surface localisation of iRhom2 variants (with
885 HA tag) in cells stably expressing the indicated murine constructs were measured by flow cytometry.
886 For quantification, the geometric mean of the specific fluorescence signal was determined. n > 11. **(C)**
887 Surface localisation of iRhom2 variants (with HA tag) in cells stably expressing the indicated human
888 constructs were measured by flow cytometry. For quantification, the geometric mean of the specific
889 fluorescence signal was determined. n > 5. **(D)** Immunoblot of samples from MEFs deficient for iRhom1
890 and iRhom2 stably expressing the indicated iRhom2 variants or GFP (ctr.) were used. The transferrin
891 receptor (TfR1) served as an input control. (n = 3). **(E)** To analyse the fate of mature ADAM17 in cells
892 expressing the indicated TOC mutations, cells were treated with bafilomycin ("B") for 8 h to inhibit
893 lysosomal degradation. Levels of mature ADAM17 were assessed by densitometric measurements and
894 calculation of the ratio between mature ADAM17 and the loading control GAPDH, which is independent
895 of lysosomal degradation. (n > 4). **(F)** To assess the turn-over rate of ADAM17 a cycloheximide-based
896 (Chx) pulse-chase experiment was performed. Reduction of ADAM17 levels was assessed by
897 densitometric measurements and normalisation to 0 h Chx treatment (set to 1). (n = 5).

898 **Figure S4: (A)** ADAM17 levels of immunoblot (Fig. 6C) were assessed by densitometric measurements
899 and calculation of the ratio between total ADAM17 (mature plus immature ADAM17) divided by the
900 respective input control. Values were normalised to the respective wt-iRhom2 sample. n > 5. **(B-C)** To
901 analyse interaction between ADAM17 and the indicated iRhom2 variants, coIPs were performed using
902 the iRhom variants (with HA tag) as bait. Immunoblotting and subsequent densitometric
903 measurements were used to quantitatively analyse iRhom2-ADAM17 binding (ratio of co-precipitated
904 ADAM17 and precipitated iRhom2) and normalised to wt-iRhom2. **(B)** MEFs from mice deficient for
905 iRhom1 and iRhom2 stably expressing indicated iRhom2 variants with ER retention signal KDEL or GFP
906 (ctr.) were used (n = 4). **(C)** iRhom-ADAM17 binding after lysosomal inhibition was analysed.
907 Densitometric measurements of coIP immunoblot (Fig. 6D) (n = 4).

908

909

910 **References**

911 Abd Alla, J., et al. (2016). J Biol Chem **291**(6): 2583-2600 DOI: 10.1074/jbc.M115.702688.

Adrain, C., et al. (2012). Science **335**(6065): 225-228 DOI: 10.1126/science.1214400.
Alcendor, R. R., et al. (2007). Circ Res **100**(10): 1512-1521 DOI: 10.1161/01.RES.0000267723.65696.4a.
Allende, M. L., et al. (2013). J Biol Chem **288**(25): 18381-18391 DOI: 10.1074/jbc.M113.478420.
Arakawa, K., et al. (2023). Genes Cells DOI: 10.1111/gtc.13050.
Arcidiacono, P., et al. (2018). Nat Commun **9**(1): 1021 DOI: 10.1038/s41467-018-03470-y.
Arndt, P. G., et al. (2011). PLoS One **6**(5): e19938 DOI: 10.1371/journal.pone.0019938.
Babendreyer, A., et al. (2020). Front Cardiovasc Med **7**: 610344 DOI: 10.3389/fcvm.2020.610344.
Barger, J. L., et al. (2008). PLoS One **3**(6): e2264 DOI: 10.1371/journal.pone.0002264.
Black, R. A., et al. (1997). Nature **385**(6618): 729-733 DOI: 10.1038/385729a0.
Blaydon, D. C., et al. (2011). N Engl J Med **365**(16): 1502-1508 DOI: 10.1056/NEJMoa1100721.
Blaydon, D. C., et al. (2012). Am J Hum Genet **90**(2): 340-346 DOI: 10.1016/j.ajhg.2011.12.008.
Bosse, Y., et al. (2007). Physiol Genomics **29**(2): 161-168 DOI: 10.1152/physiolgenomics.00134.2006.
Brooke, M. A., et al. (2014). Hum Mol Genet **23**(15): 4064-4076 DOI: 10.1093/hmg/ddu120.
Busch, H., et al. (2008). Mol Syst Biol **4**: 199 DOI: 10.1038/msb.2008.36.
Cavadas, M., et al. (2017). Cell Rep **21**(3): 745-757 DOI: 10.1016/j.celrep.2017.09.074.
Chao-Chu, J., et al. (2021). J Invest Dermatol **141**(4): 722-726 DOI: 10.1016/j.jid.2020.09.010.
Chen, Y., et al. (2008). BMC Genomics **9**: 264 DOI: 10.1186/1471-2164-9-264.
Christova, Y., et al. (2013). EMBO Rep **14**(10): 884-890 DOI: 10.1038/embor.2013.128.
Dosztanyi, Z., et al. (2009). Bioinformatics **25**(20): 2745-2746 DOI: 10.1093/bioinformatics/btp518.
Dufour, C. R., et al. (2007). Cell Metab **5**(5): 345-356 DOI: 10.1016/j.cmet.2007.03.007.
Dulloo, I., et al. (2022). bioRxiv: 2022.2011.2028.518246 DOI: 10.1101/2022.11.28.518246.
Düsterhöft, S., et al. (2021). Cell Mol Life Sci DOI: 10.1007/s00018-021-03845-3.
Dyson, H. J. (2016). Biophys J **110**(5): 1013-1016 DOI: 10.1016/j.bpj.2016.01.030.
Ellis, A., et al. (1994). Eur J Cancer B Oral Oncol **30B**(2): 102-112 DOI: 10.1016/0964-1955(94)90061-2.
Ellis, A., et al. (2015). Orphanet J Rare Dis **10**: 126 DOI: 10.1186/s13023-015-0346-2.
Erdos, G., et al. (2021). Nucleic Acids Res **49**(W1): W297-W303 DOI: 10.1093/nar/gkab408.
Esaki, H., et al. (2015). J Allergy Clin Immunol **135**(1): 153-163 DOI: 10.1016/j.jaci.2014.10.037.
Gambino, V., et al. (2013). Aging Cell **12**(3): 435-445 DOI: 10.1111/acel.12060.
Garinis, G. A., et al. (2009). Nat Cell Biol **11**(5): 604-615 DOI: 10.1038/ncb1866.
Giese, A. A., et al. (2021). Sci Rep **11**(1): 24230 DOI: 10.1038/s41598-021-03522-2.
Grieve, A., et al. (2017). Elife **6** DOI: 10.7554/eLife.23968.
Guo, A., et al. (2014). Mol Cell Proteomics **13**(1): 372-387 DOI: 10.1074/mcp.O113.027870.
Henrichsen, C. N., et al. (2011). PLoS Comput Biol **7**(1): e1001054 DOI: 10.1371/journal.pcbi.1001054.
Ho, S. N., et al. (1989). Gene **77**(1): 51-59 DOI: 10.1016/0378-1119(89)90358-2.
Hornbeck, P. V., et al. (2015). Nucleic Acids Res **43**(Database issue): D512-520 DOI: 10.1093/nar/gku1267.
Hosur, V., et al. (2018a). FEBS Open Bio **8**(4): 702-710 DOI: 10.1002/2211-5463.12407.
Hosur, V., et al. (2018b). Front Genet **9**: 233 DOI: 10.3389/fgene.2018.00233.
Hosur, V., et al. (2014). Proc Natl Acad Sci U S A **111**(21): E2200-2209 DOI: 10.1073/pnas.1323908111.
Hosur, V., et al. (2017). Biol Open **6**(8): 1174-1179 DOI: 10.1242/bio.026260.
Howel-Evans, W., et al. (1958). Q J Med **27**(107): 413-429.
Hruz, T., et al. (2008). Adv Bioinformatics **2008**: 420747 DOI: 10.1155/2008/420747.
Inada, M., et al. (2016). Int J Mol Med **37**(6): 1521-1527 DOI: 10.3892/ijmm.2016.2568.
Issuree, P. D., et al. (2013). J Clin Invest **123**(2): 928-932 DOI: 10.1172/JCI66168.
Jocher, G., et al. (2022). EMBO Rep **23**(6): e54305 DOI: 10.15252/embr.202154305.
Johnson, K. R., et al. (2003). Genomics **81**(1): 6-14 DOI: 10.1016/S0888-7543(02)00013-7.
Jumper, J., et al. (2021). Nature **596**(7873): 583-589 DOI: 10.1038/s41586-021-03819-2.
Kahveci-Türköz, S., et al. (2023). Cell Mol Life Sci **80**(5): 135 DOI: 10.1007/s00018-023-04783-y.
Ketteler, R., et al. (2002). Gene Ther **9**(8): 477-487 DOI: 10.1038/sj.gt.3301653.
Klausen, M. S., et al. (2019). Proteins **87**(6): 520-527 DOI: 10.1002/prot.25674.
Kubo, S., et al. (2022). Nat Immunol **23**(1): 75-85 DOI: 10.1038/s41590-021-01093-y.

964 Künzel, U., et al. (2018). Elife **7** DOI: 10.7554/eLife.35012.
965 Lambert, D. W., et al. (2005). J Biol Chem **280**(34): 30113-30119 DOI: 10.1074/jbc.M505111200.
966 Lattin, J. E., et al. (2008). Immunome Res **4**: 5 DOI: 10.1186/1745-7580-4-5.
967 Li, X., et al. (2017). J Cell Sci **130**(5): 868-878 DOI: 10.1242/jcs.196436.
968 Li, X., et al. (2015). Proc Natl Acad Sci U S A **112**(19): 6080-6085 DOI: 10.1073/pnas.1505649112.
969 Lu, X. L., et al. (2017). Biomed Pharmacother **86**: 645-653 DOI: 10.1016/j.biopha.2016.11.075.
970 Lucas, E., et al. (2014). Biochim Biophys Acta **1842**(12 Pt A): 2448-2456 DOI:
971 10.1016/j.bbadis.2014.09.004.
972 Maney, S. K., et al. (2015). Sci Signal **8**(401): ra109 DOI: 10.1126/scisignal.aac5356.
973 Marchina, E., et al. (2014). J Neurol Sci **337**(1-2): 42-46 DOI: 10.1016/j.jns.2013.11.014.
974 Maretzky, T., et al. (2013). Proc Natl Acad Sci U S A **110**(28): 11433-11438 DOI:
975 10.1073/pnas.1302553110.
976 Maruthappu, T., et al. (2017). Nat Commun **8**: 14174 DOI: 10.1038/ncomms14174.
977 McIlwain, D. R., et al. (2012). Science **335**(6065): 229-232 DOI: 10.1126/science.1214448.
978 Mercader, J. M., et al. (2012). PLoS Genet **8**(12): e1003046 DOI: 10.1371/journal.pgen.1003046.
979 Meszaros, B., et al. (2018). Nucleic Acids Res **46**(W1): W329-W337 DOI: 10.1093/nar/gky384.
980 Meszaros, B., et al. (2009). PLoS Comput Biol **5**(5): e1000376 DOI: 10.1371/journal.pcbi.1000376.
981 Mirdita, M., et al. (2022). Nat Methods **19**(6): 679-682 DOI: 10.1038/s41592-022-01488-1.
982 Mokoena, T., et al. (2018). Clin Genet **93**(5): 1114-1116 DOI: 10.1111/cge.13161.
983 Muchir, A., et al. (2007). Hum Mol Genet **16**(15): 1884-1895 DOI: 10.1093/hmg/ddm137.
984 Nguyen Ba, A. N., et al. (2009). BMC Bioinformatics **10**: 202 DOI: 10.1186/1471-2105-10-202.
985 Niehues, R. V., et al. (2022). FASEB J **36**(3): e22234 DOI: 10.1096/fj.202101521R.
986 Oikonomidi, I., et al. (2018). Elife **7** DOI: 10.7554/eLife.35032.
987 Oka, S., et al. (2011). Cell Metab **14**(5): 598-611 DOI: 10.1016/j.cmet.2011.10.001.
988 Palau, V., et al. (2020). Nephrol Dial Transplant **35**(6): 1071-1072 DOI: 10.1093/ndt/gfaa093.
989 Peschon, J. J., et al. (1998). Science **282**(5392): 1281-1284 DOI: 10.1126/science.282.5392.1281.
990 Qu, L., et al. (2019). Acta Derm Venereol **99**(7): 699-700 DOI: 10.2340/00015555-3189.
991 Rabinowitsch, A. I., et al. (2023). J Cell Sci DOI: 10.1242/jcs.260910.
992 Ramchandran, R., et al. (2006). Proc Natl Acad Sci U S A **103**(50): 19087-19092 DOI:
993 10.1073/pnas.0602715103.
994 Ricard, G., et al. (2010). PLoS Biol **8**(11): e1000543 DOI: 10.1371/journal.pbio.1000543.
995 Rizza, S., et al. (2015). Atherosclerosis **239**(2): 459-464 DOI: 10.1016/j.atherosclerosis.2015.01.029.
996 Roth, R. B., et al. (2006). Neurogenetics **7**(2): 67-80 DOI: 10.1007/s10048-006-0032-6.
997 Ruijter, J. M., et al. (2009). Nucleic Acids Res **37**(6): e45 DOI: 10.1093/nar/gkp045.
998 Sa, S. M., et al. (2007). J Immunol **178**(4): 2229-2240 DOI: 10.4049/jimmunol.178.4.2229.
999 Saarinen, S., et al. (2012). Fam Cancer **11**(3): 525-528 DOI: 10.1007/s10689-012-9532-8.
1000 Sahin, U., et al. (2004). J Cell Biol **164**(5): 769-779 DOI: 10.1083/jcb.200307137.
1001 Sato, T., et al. (2013). Sci Rep **3**: 1911 DOI: 10.1038/srep01911.
1002 Schmitt, L., et al. (2018). Lasers Med Sci **33**(4): 765-772 DOI: 10.1007/s10103-017-2409-1.
1003 Schumacher, N., et al. (2023). Biochim Biophys Acta Mol Cell Res: 119489 DOI:
1004 10.1016/j.bbamcr.2023.119489.
1005 Shalhoub, V., et al. (2010). J Cell Biochem **111**(4): 911-921 DOI: 10.1002/jcb.22779.
1006 Shuai, Y., et al. (2011). Toxicol Lett **200**(1-2): 77-87 DOI: 10.1016/j.toxlet.2010.10.017.
1007 Sieber, B., et al. (2022). J Cell Sci **135**(17) DOI: 10.1242/jcs.259949.
1008 Sievers, F., et al. (2011). Mol Syst Biol **7**: 539 DOI: 10.1038/msb.2011.75.
1009 Siggs, O. M., et al. (2014). Biol Open **3**(12): 1151-1157 DOI: 10.1242/bio.201410116.
1010 Siggs, O. M., et al. (2012). Blood **119**(24): 5769-5771 DOI: 10.1182/blood-2012-03-417949.
1011 Smith, J. C., et al. (2008). J Invest Dermatol **128**(5): 1298-1310 DOI: 10.1038/sj.jid.5701149.
1012 Smyth, E. C., et al. (2017). Nat Rev Dis Primers **3**: 17048 DOI: 10.1038/nrdp.2017.48.
1013 Strunnikova, N. V., et al. (2009). PLoS One **4**(12): e8402 DOI: 10.1371/journal.pone.0008402.
1014 Swindell, W. R., et al. (2012). PLoS One **7**(3): e34594 DOI: 10.1371/journal.pone.0034594.
1015 Tang, B., et al. (2020). FASEB J **34**(4): 4956-4969 DOI: 10.1096/fj.201902649R.

Thorrez, L., et al. (2008). PLoS One **3**(3): e1854 DOI: 10.1371/journal.pone.0001854.
Traister, A., et al. (2013). PLoS One **8**(11): e77331 DOI: 10.1371/journal.pone.0077331.
Uhlenhopp, D. J., et al. (2020). Clin J Gastroenterol **13**(6): 1010-1021 DOI: 10.1007/s12328-020-01237-x.
Vallender, T. W. and B. T. Lahn (2006). FEBS Lett **580**(18): 4560-4566 DOI: 10.1016/j.febslet.2006.07.017.
Verkerk, A. J., et al. (2009). Am J Hum Genet **85**(1): 40-52 DOI: 10.1016/j.ajhg.2009.06.004.
Visser, R., et al. (2012). PLoS One **7**(11): e49229 DOI: 10.1371/journal.pone.0049229.
Voets, A. M., et al. (2012). Biochim Biophys Acta **1822**(7): 1161-1168 DOI: 10.1016/j.bbadis.2011.10.009.
Wang, L., et al. (2016). Sci Rep **6**: 28399 DOI: 10.1038/srep28399.
Wang, Q., et al. (2013). BMC Cancer **13**: 137 DOI: 10.1186/1471-2407-13-137.
Wang, X. M., et al. (2012). Stem Cell Res Ther **3**(5): 39 DOI: 10.1186/scrt130.
Wong, J., et al. (2010). Crit Care Med **38**(1): 25-31 DOI: 10.1097/CCM.0b013e3181b427e8.
Yang, T., et al. (2022). J Transl Med **20**(1): 127 DOI: 10.1186/s12967-022-03311-z.
Yuan, F., et al. (2021). PLoS Pathog **17**(3): e1009393 DOI: 10.1371/journal.ppat.1009393.
Yunoki, T., et al. (2018). Oncol Lett **16**(5): 6729-6734 DOI: 10.3892/ol.2018.9484.
Zanotti, A., et al. (2022). Science **378**(6623): 996-1000 DOI: 10.1126/science.abo5672.
Zaruba, M., et al. (2022). Viruses **14**(2) DOI: 10.3390/v14020381.
Zhao, Y., et al. (2007). Cell **129**(2): 303-317 DOI: 10.1016/j.cell.2007.03.030.

Figure 1

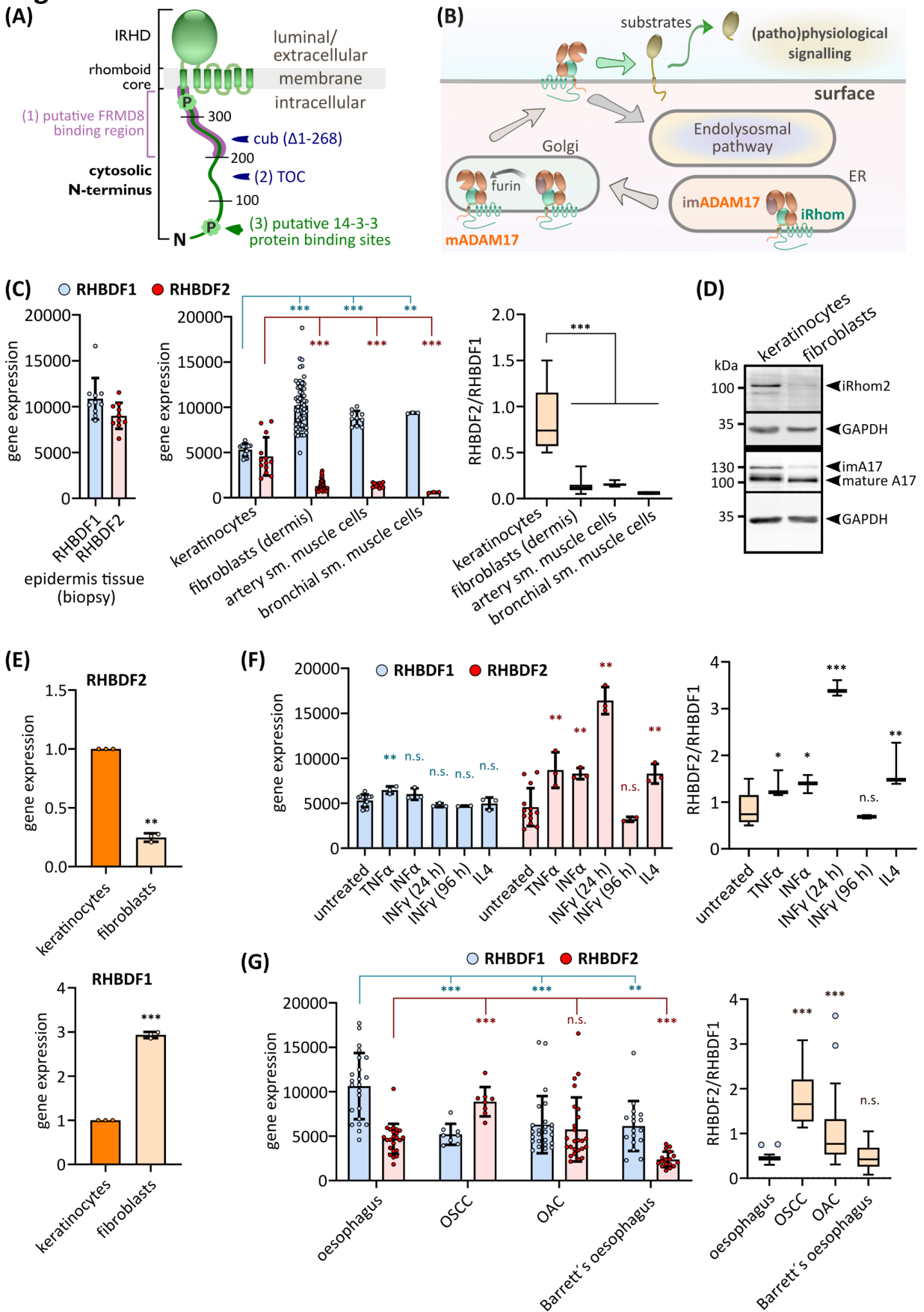
(A)
IRHD
luminal/ extracellular
rhomboid core
membrane
intracellular
(1) putative FRMD8 binding region
300
cub (Δ1-268)
200
(2) TOC
cytosolic N-terminus
100
(3) putative 14-3-3 protein binding sites
N
(B)
substrates
(patho)physiological signalling
surface
Endolysosmal pathway
Golgi
furin
ER
imADAM17
iRhom
mADAM17
(C)
RHBDF1
RHBDF2
gene expression
RHBDF1
RHBDF2
epidermis tissue (biopsy)
keratinocytes
fibroblasts (dermis)
artery sm. muscle cells
bronchial sm. muscle cells
RHBDF2/RHBDF1
(D)
keratinocytes
fibroblasts
kDa
iRhom2
GAPDH
imA17
mature A17
GAPDH
(E)
RHBDF2
RHBDF1
keratinocytes
fibroblasts
(F)
untreated
TNFα
INFα
INFγ (24 h)
INFγ (96 h)
IL4
n.s.
(G)
oesophagus
OSCC
OAC
Barrett´s oesophagus

Figure 2

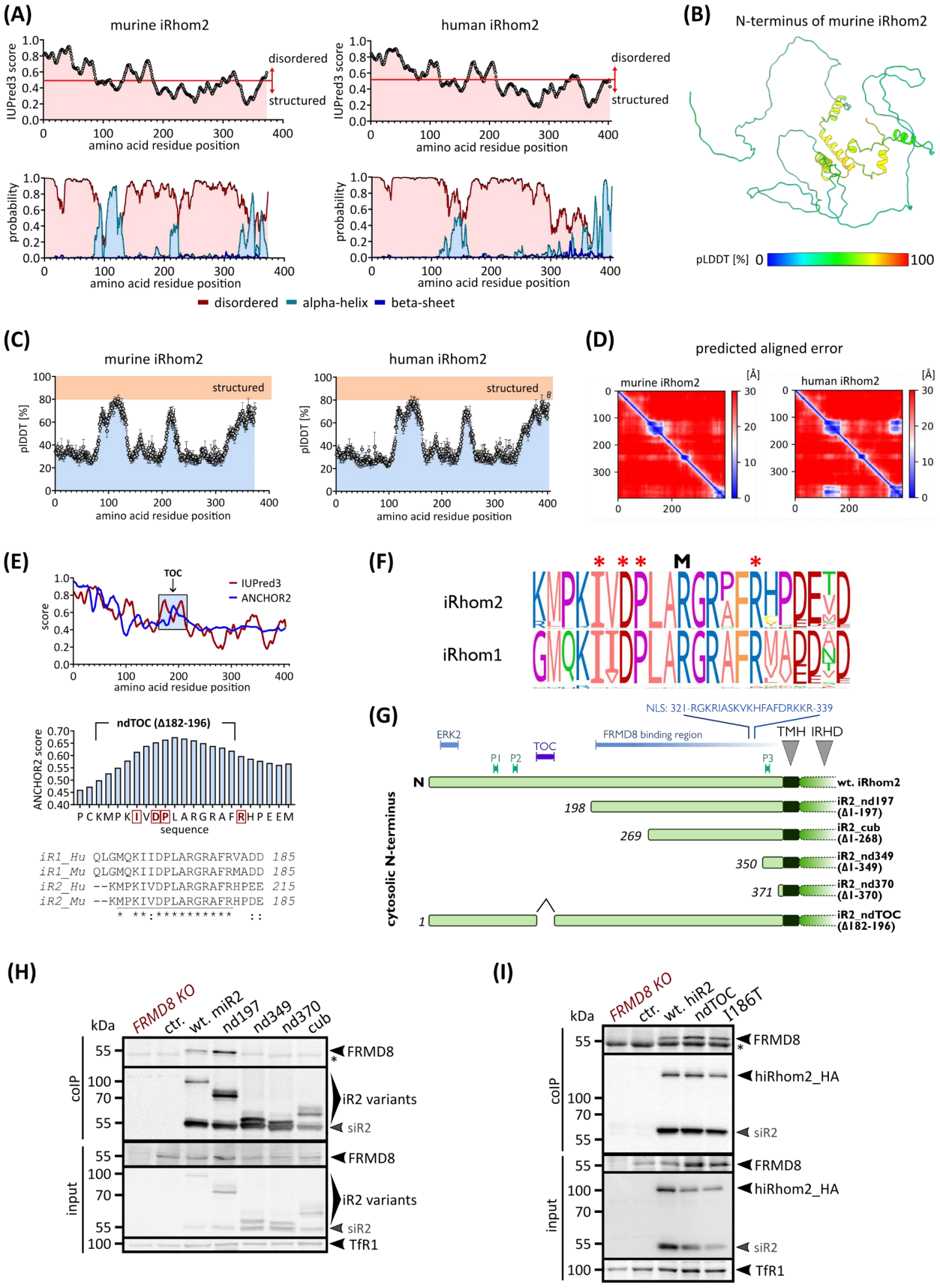
(A)
murine iRhom2
human iRhom2
IUPred3 score
disordered
structured
amino acid residue position
probability
disordered
alpha-helix
beta-sheet
(B)
N-terminus of murine iRhom2
pLDDT [%]
0
100
(C)
murine iRhom2
human iRhom2
pIDDT [%]
structured
amino acid residue position
(D)
predicted aligned error
murine iRhom2
human iRhom2
[Å]
(E)
TOC
IUPred3
ANCHOR2
score
amino acid residue position
ndTOC (Δ182-196)
ANCHOR2 score
P C K M P K I V D P L A R G R A F R H P E E M
sequence
iR1_Hu QLGMQKIIDPLARGRAFRVADD 185
iR1_Mu QLGMQKIIDPLARGRAFRMADD 185
iR2_Hu --KMPKIVDPLARGRAFRHPEE 215
iR2_Mu --KMPKIVDPLARGRAFRHPDE 185
(F)
iRhom2
iRhom1
(G)
NLS: 321-RGKRIASKVKHFAFDRKKR-339
ERK2
FRMD8 binding region
TMH
IRHD
TOC
P1
P2
P3
N
cytosolic N-terminus
wt. iRhom2
198
iR2_nd197 (Δ1-197)
269
iR2_cub (Δ1-268)
350
iR2_nd349 (Δ1-349)
371
iR2_nd370 (Δ1-370)
1
iR2_ndTOC (Δ182-196)
(H)
kDa
FRMD8 KO
ctr.
wt. miR2
nd197
nd349
nd370
cub
coIP
input
FRMD8
iR2 variants
siR2
TfR1
(I)
kDa
FRMD8 KO
ctr.
wt. hiR2
ndTOC
I186T
coIP
input
FRMD8
hiRhom2_HA
siR2
TfR1

Figure 3

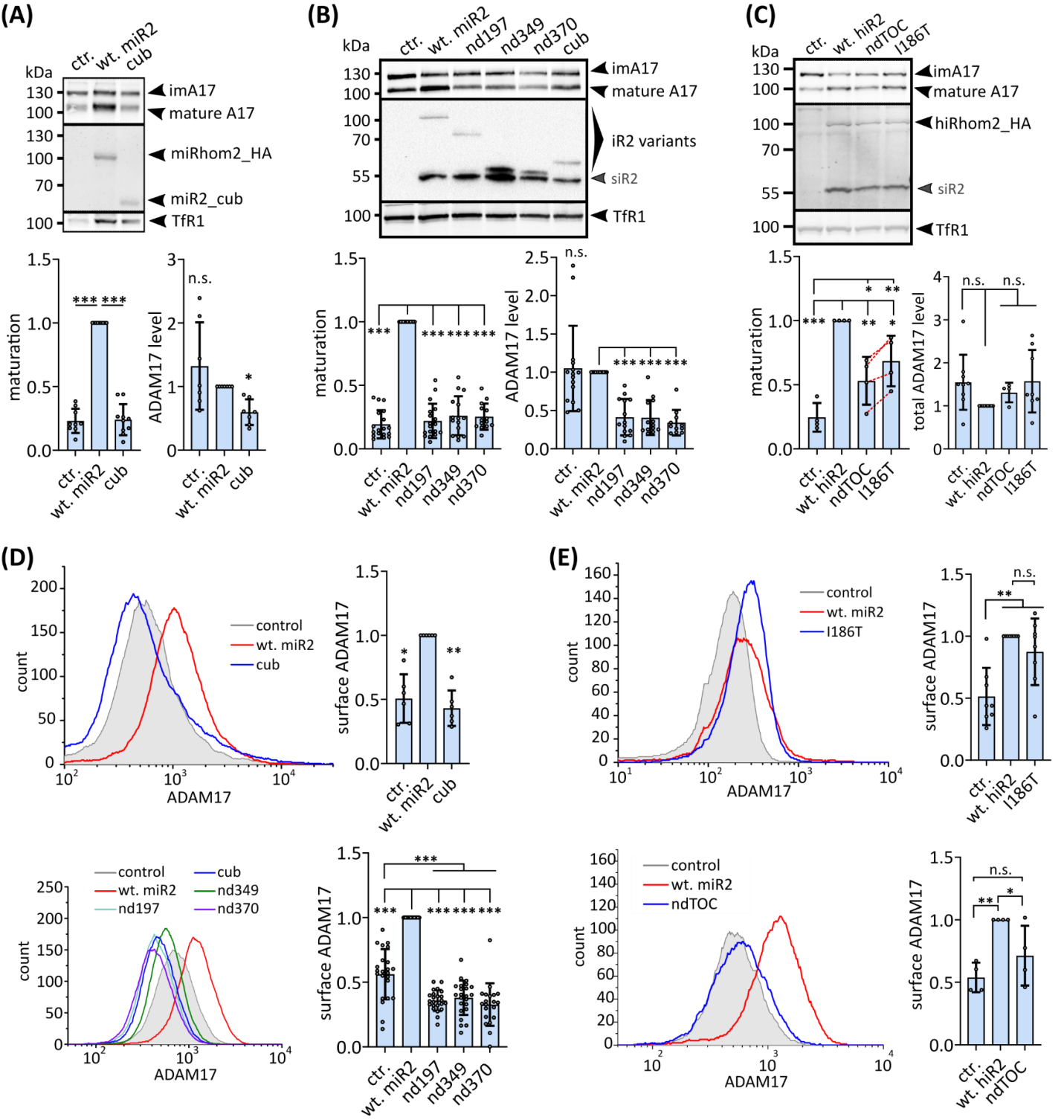
(A)
ctr.
wt. miR2
cub
kDa
130
100
imA17
mature A17
miRhom2_HA
70
miR2_cub
TfR1
maturation
ADAM17 level
n.s.
(B)
nd197
nd349
nd370
iR2 variants
siR2
(C)
wt. hiR2
ndTOC
I186T
hiRhom2_HA
total ADAM17 level
(D)
control
count
ADAM17
surface ADAM17
(E)

Figure 4

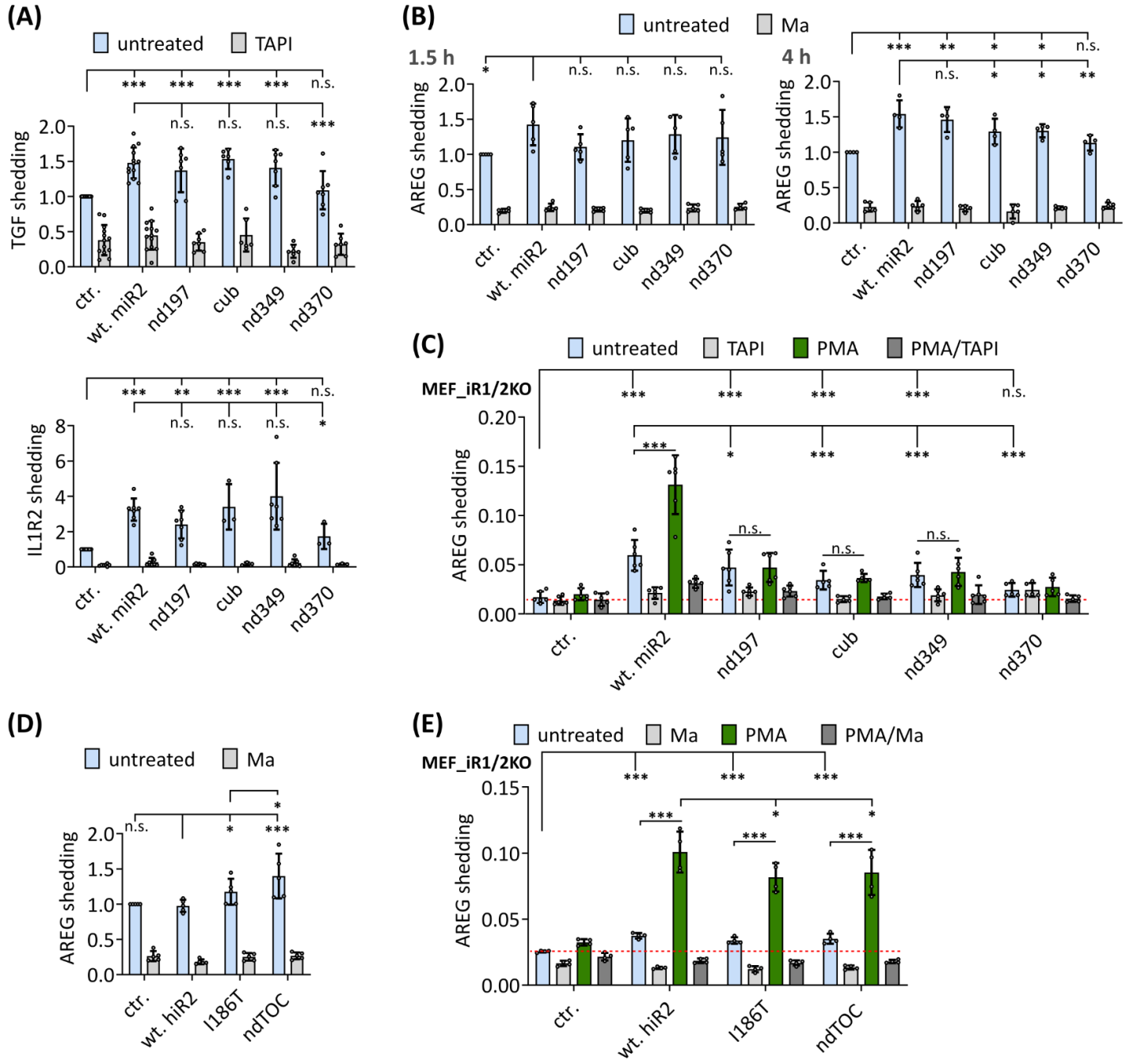
(A)
untreated
TAPI
TGF shedding
IL1R2 shedding
ctr.
wt. miR2
nd197
cub
nd349
nd370
(B)
untreated
Ma
1.5 h
4 h
AREG shedding
(C)
untreated
TAPI
PMA
PMA/TAPI
MEF_iR1/2KO
AREG shedding
(D)
untreated
Ma
AREG shedding
ctr.
wt. hiR2
I186T
ndTOC
(E)
untreated
Ma
PMA
PMA/Ma
MEF_iR1/2KO
AREG shedding

Figure 5

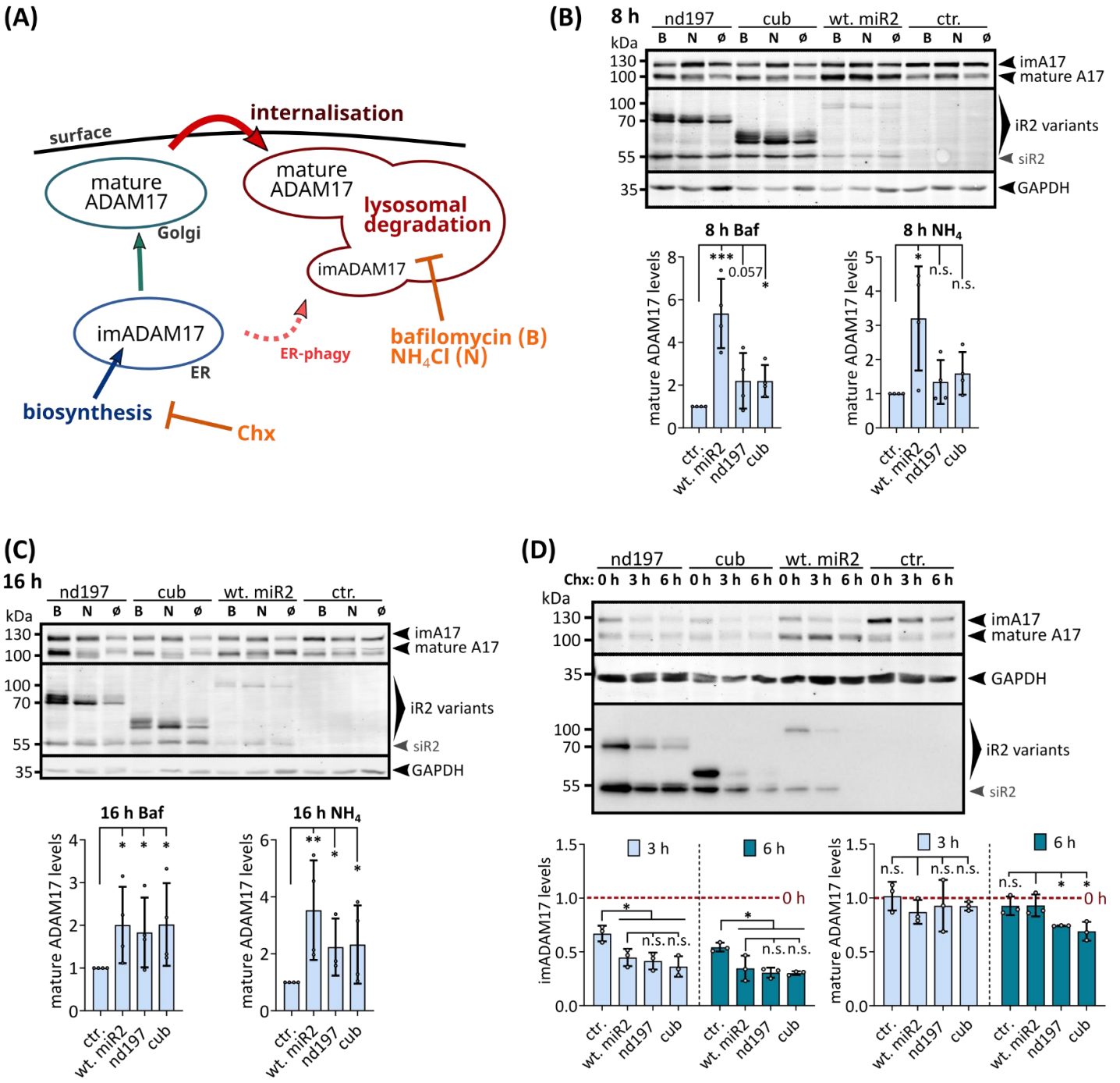
(A)
surface
internalisation
mature ADAM17
Golgi
mature ADAM17
lysosomal degradation
imADAM17
imADAM17
ER
ER-phagy
bafilomycin (B)
NH4Cl (N)
biosynthesis
Chx
(B)
8 h
nd197
cub
wt. miR2
ctr.
B N ø B N ø B N ø B N ø
kDa
130
100
100
70
55
35
imA17
mature A17
iR2 variants
siR2
GAPDH
8 h Baf
8 h NH4
mature ADAM17 levels
***
0.057
*
n.s.
ctr.
wt. miR2
nd197
cub
(C)
16 h
nd197
cub
wt. miR2
ctr.
B N ø B N ø B N ø B N ø
kDa
130
100
100
70
55
35
imA17
mature A17
iR2 variants
siR2
GAPDH
16 h Baf
16 h NH4
mature ADAM17 levels
**
*
ctr.
wt. miR2
nd197
cub
(D)
nd197
cub
wt. miR2
ctr.
Chx: 0 h 3 h 6 h 0 h 3 h 6 h 0 h 3 h 6 h 0 h 3 h 6 h
kDa
130
100
35
100
70
55
imA17
mature A17
GAPDH
iR2 variants
siR2
3 h
6 h
imADAM17 levels
mature ADAM17 levels
0 h
n.s.
*
ctr.
wt. miR2
nd197
cub

Figure 6

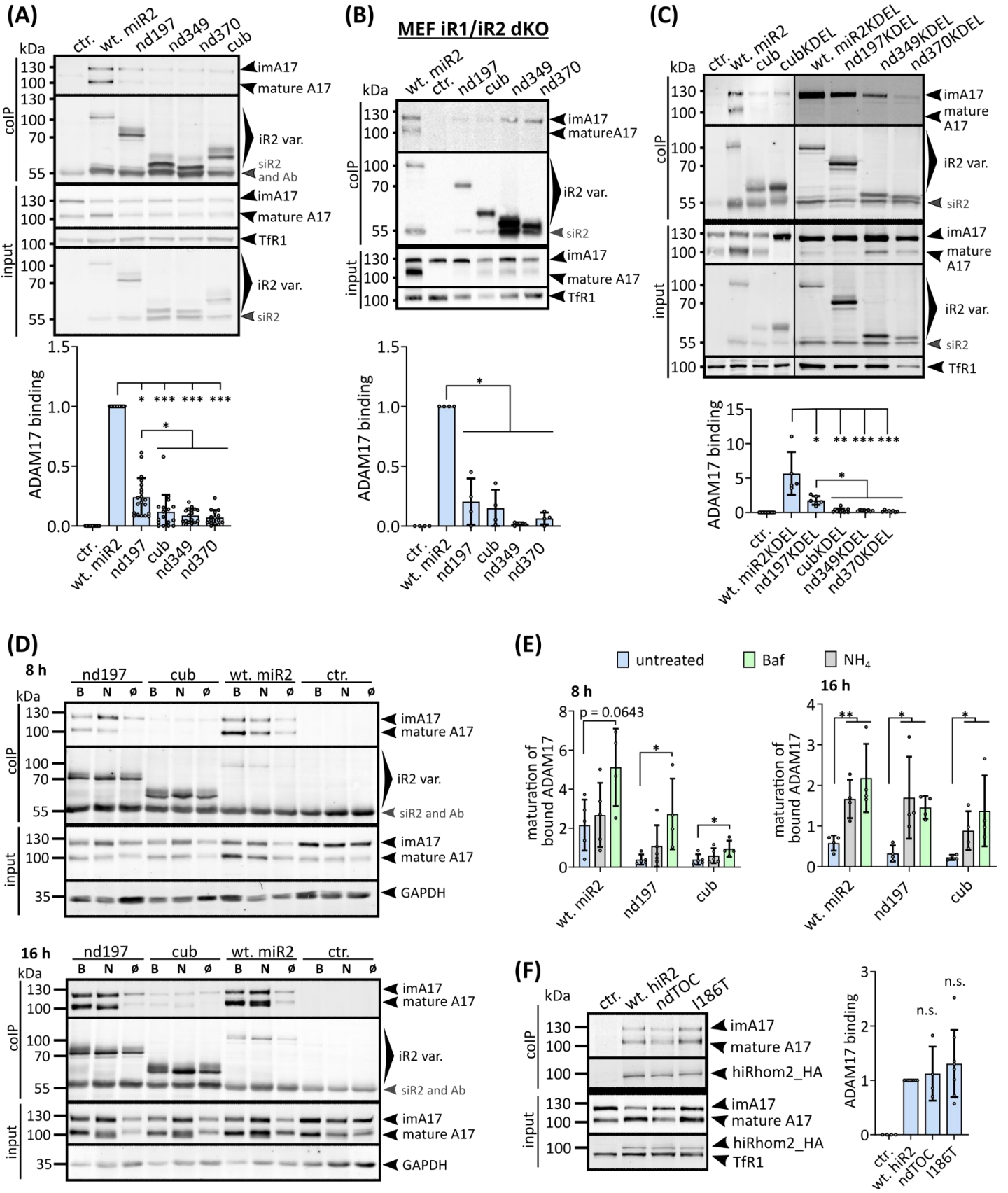
(A)
ctr.
wt. miR2
nd197
nd349
nd370
cub
kDa
130
100
70
55
colP
input
imA17
mature A17
iR2 var.
siR2 and Ab
TfR1
siR2
ADAM17 binding
(B)
MEF iR1/iR2 dKO
wt. miR2
ctr.
nd197
cub
nd349
nd370
matureA17
(C)
cubKDEL
wt. miR2KDEL
nd197KDEL
nd349KDEL
nd370KDEL
wt. miR2KDEL
nd197KDEL
cubKDEL
nd349KDEL
nd370KDEL
(D)
8 h
16 h
B
N
ø
GAPDH
35
(E)
untreated
Baf
NH4
p = 0.0643
maturation of bound ADAM17
(F)
wt. hiR2
ndTOC
I186T
hiRhom2_HA
n.s.

Figure 7

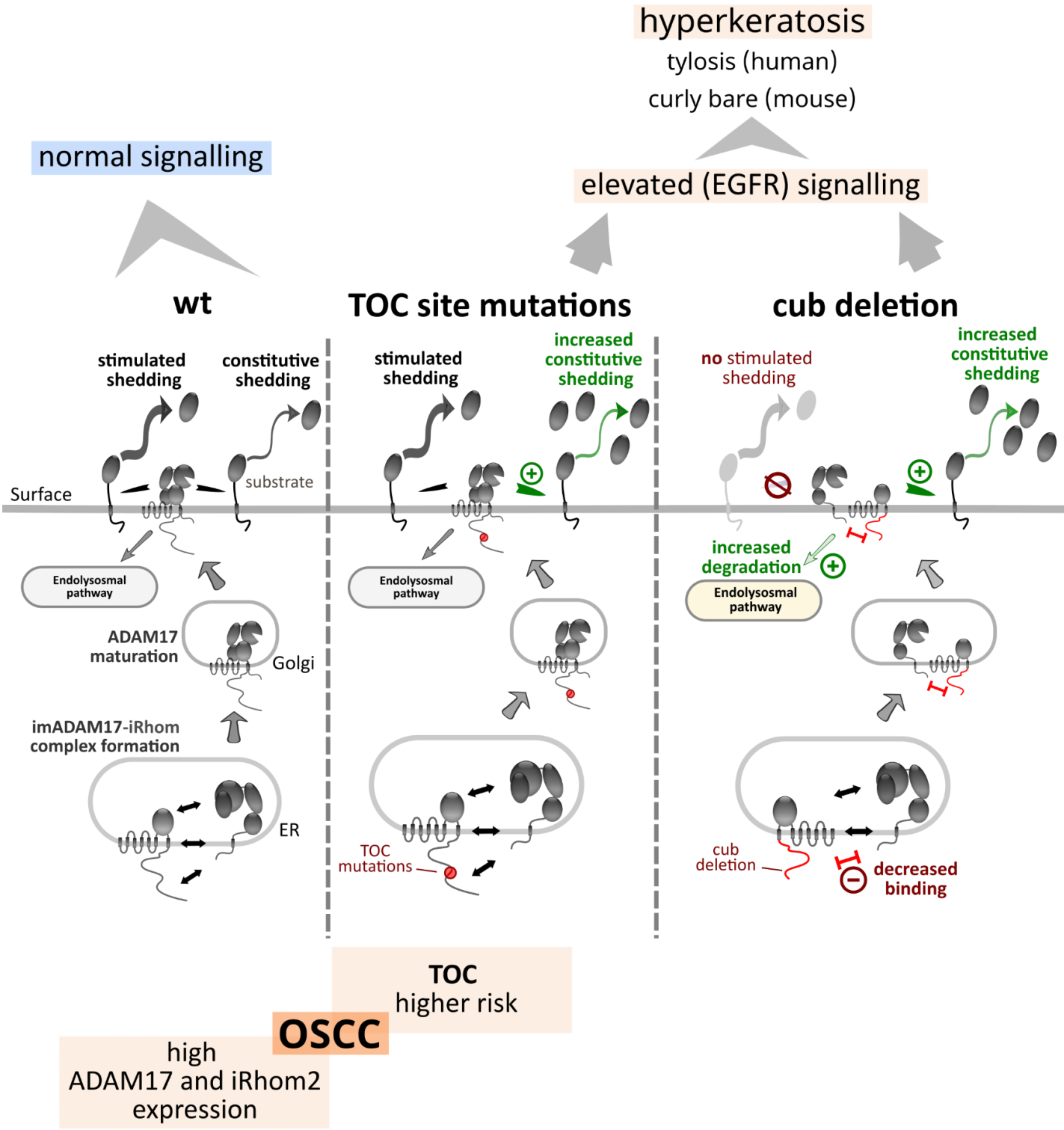
hyperkeratosis
tylosis (human)
curly bare (mouse)
normal signalling
elevated (EGFR) signalling
wt
TOC site mutations
cub deletion
stimulated shedding
constitutive shedding
substrate
Surface
Endolysosmal pathway
ADAM17 maturation
Golgi
imADAM17-iRhom complex formation
ER
stimulated shedding
increased constitutive shedding
Endolysosmal pathway
TOC mutations
no stimulated shedding
increased constitutive shedding
increased degradation
Endolysosmal pathway
cub deletion
decreased binding
TOC
higher risk
OSCC
high
ADAM17 and iRhom2
expression

Figure S1

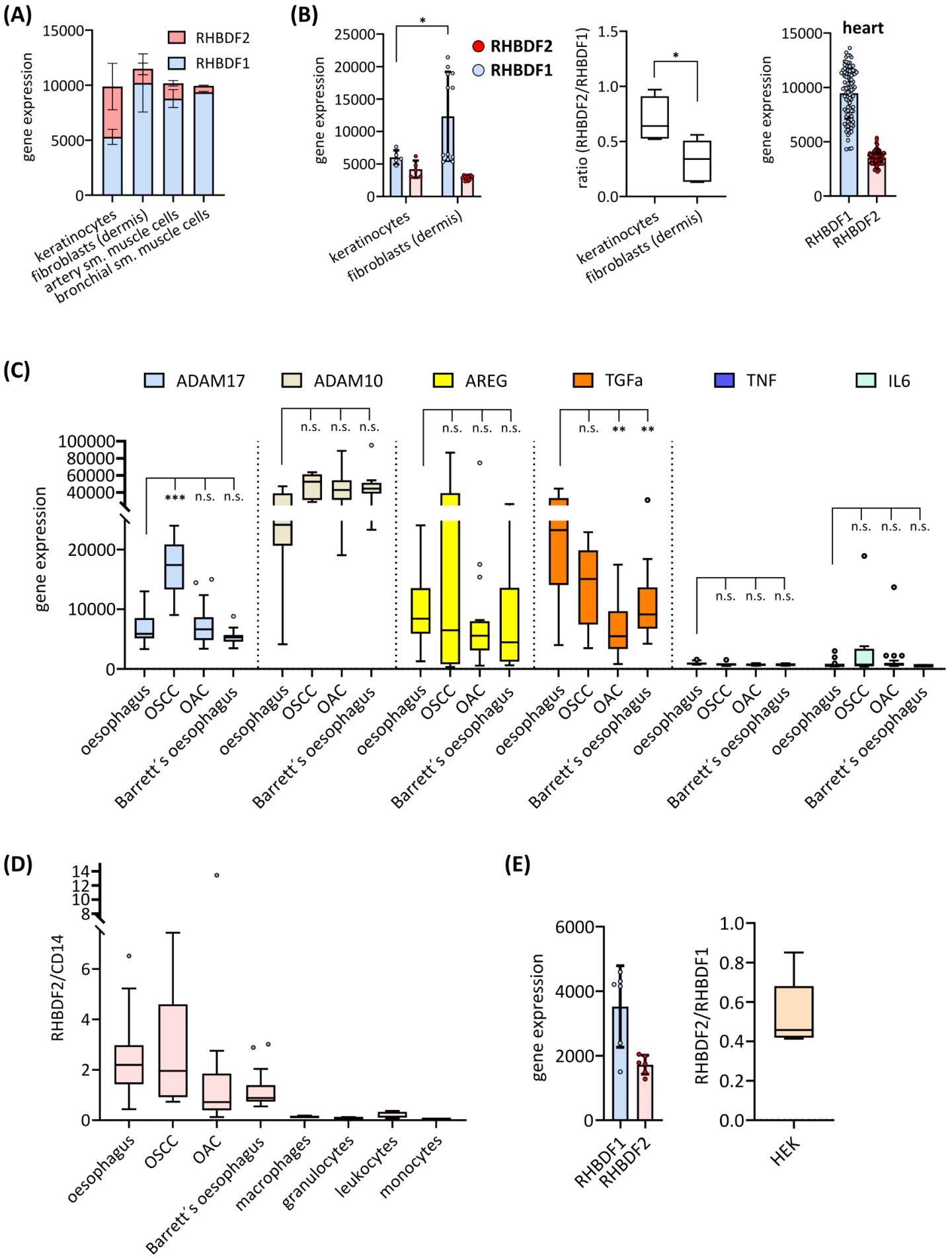
(A)
RHBDF2
RHBDF1
gene expression
keratinocytes
fibroblasts (dermis)
artery sm. muscle cells
bronchial sm. muscle cells
(B)
RHBDF2
RHBDF1
gene expression
ratio (RHBDF2/RHBDF1)
heart
keratinocytes
fibroblasts (dermis)
RHBDF1
RHBDF2
(C)
ADAM17
ADAM10
AREG
TGFa
TNF
IL6
gene expression
n.s.
***
**
oesophagus
OSCC
OAC
Barrett´s oesophagus
(D)
RHBDF2/CD14
oesophagus
OSCC
OAC
Barrett´s oesophagus
macrophages
granulocytes
leukocytes
monocytes
(E)
gene expression
RHBDF1
RHBDF2
RHBDF2/RHBDF1
HEK

Figure S2

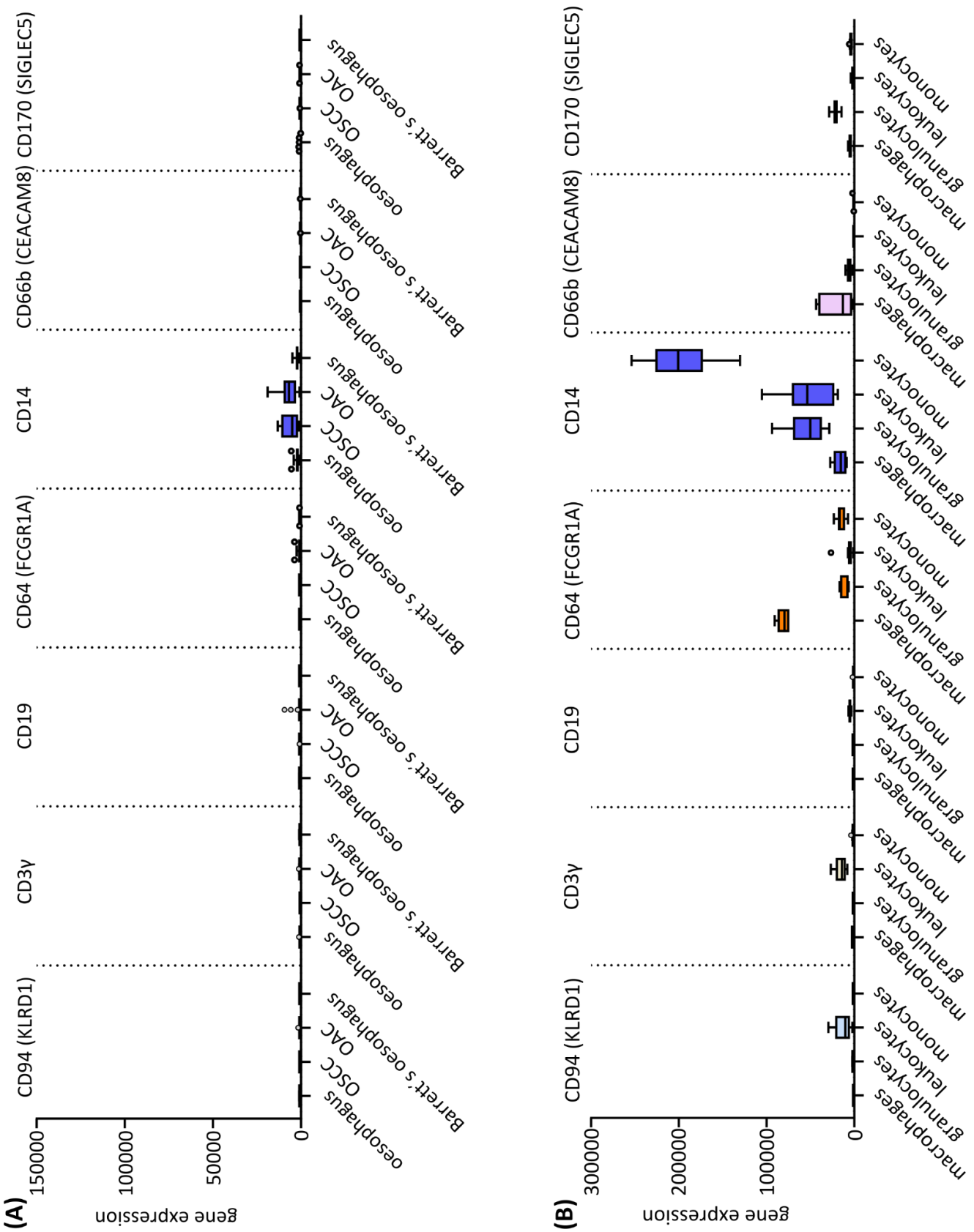
(A)
gene expression
150000
100000
50000
0
CD94 (KLRD1)
CD3γ
CD19
CD64 (FCGR1A)
CD14
CD66b (CEACAM8)
CD170 (SIGLEC5)
oesophagus
OSCC
OAC
Barrett's oesophagus
(B)
gene expression
300000
200000
100000
0
CD94 (KLRD1)
CD3γ
CD19
CD64 (FCGR1A)
CD14
CD66b (CEACAM8)
CD170 (SIGLEC5)
macrophages
granulocytes
leukocytes
monocytes

Figure S3

(A)

```
muiR2          1 MASADKNGSNLPSVSGSRLQSRKPPNLSITIPPP--ESQAPGEQDSMLPE----------
huiR2iso1      1 MASADKNGGSVSSVSSSRLQSRKPPNLSITIPPPEKETQAPGEQDSMLPEGFQNRRLKKS
huiR2iso2      1 MASADKNGGSVSSVSSSRLQSRKPPNLSITIPPPEKETQAPGEQDSMLPE----------
                 ********..:.***.*****************  *:************

muiR2         61 ------------------RRKNPAYLKSVSLQEPRGRWQEGAEKRPGFRRQASLSQSIRK
huiR2iso1     61 QPRTWAAHTTACPPSFLPKRKNPAYLKSVSLQEPRSRWQESSEKRPGFRRQASLSQSIRK
huiR2iso2     61 -------------------RKNPAYLKSVSLQEPRSRWQESSEKRPGFRRQASLSQSIRK
                                    ****************.****.:*****************
```

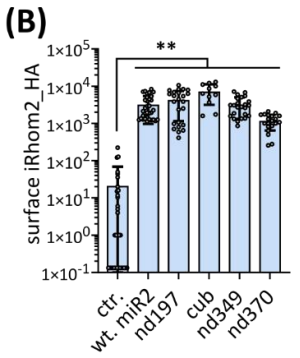

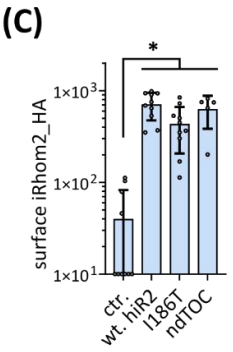

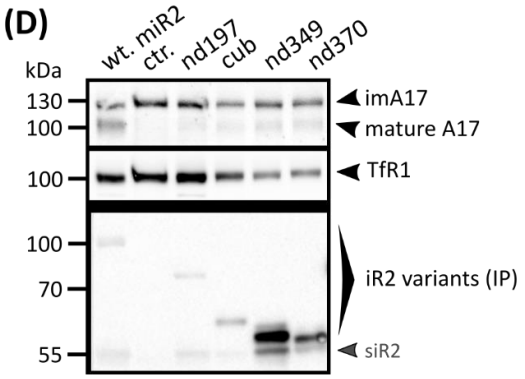

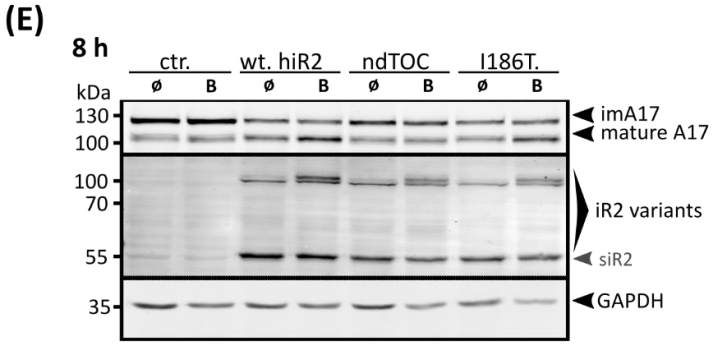

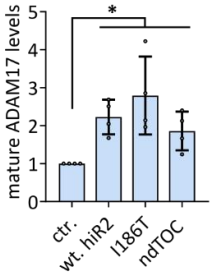

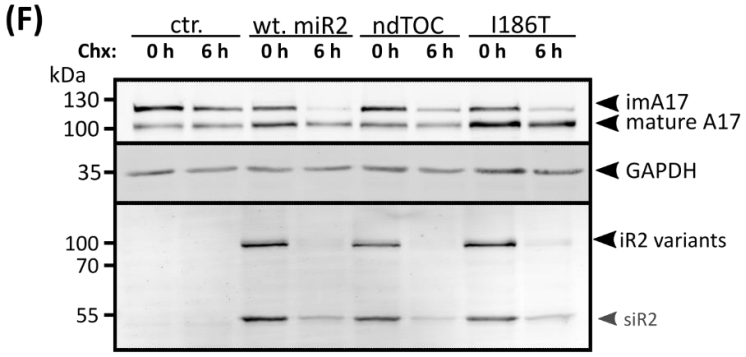

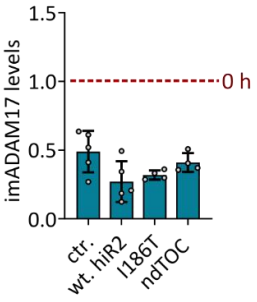

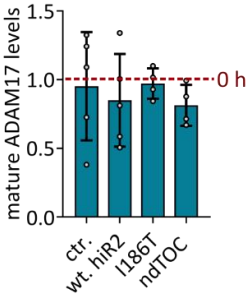

Figure S4

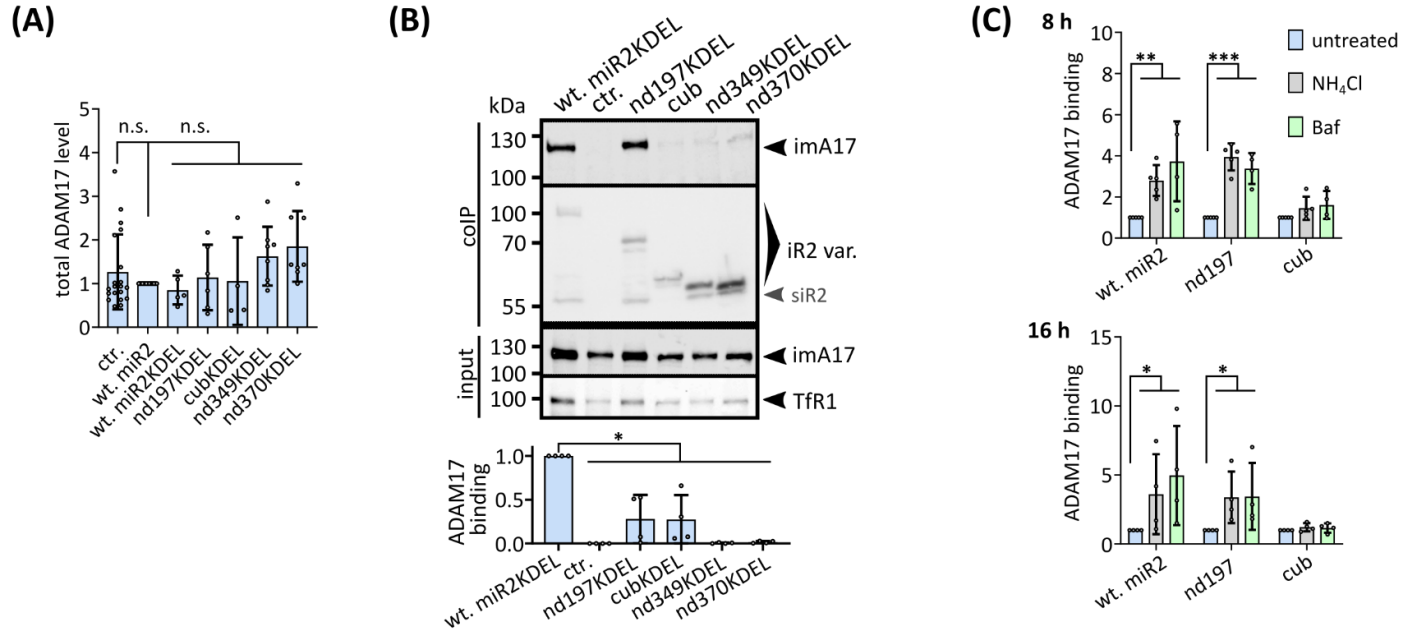
(A)
total ADAM17 level
n.s.
n.s.
ctr.
wt. miR2
wt. miR2KDEL
nd197KDEL
cubKDEL
nd349KDEL
nd370KDEL
(B)
kDa
wt. miR2KDEL
ctr.
nd197KDEL
cub
nd349KDEL
nd370KDEL
coIP
input
130
100
100
70
55
130
100
100
imA17
iR2 var.
siR2
imA17
TfR1
ADAM17 binding
*
(C)
8 h
16 h
ADAM17 binding
untreated
NH4Cl
Baf
**
***
*
*
wt. miR2
nd197
cub